JGR Planets

RESEARCH ARTICLE

10.1029/2025JE009030

Magnetic Mineralogy in Lunar Mare Basalts and Implications for Paleointensity Retrieval

Ji-In Jung[1], Sonia M. Tikoo[1,2], Zoltán Váci[3], Michael J. Krawczynski[3], Peat Solheid[4], Dale H. Burns[2,5], and Arturas Vailionis[5,6]

[1]Department of Geophysics, Stanford University, Stanford, CA, USA, [2]Department of Earth and Planetary Sciences, Stanford University, Stanford, CA, USA, [3]Department of Earth, Environmental and Planetary Sciences, Washington University in St. Louis, St. Louis, MO, USA, [4]Institute for Rock Magnetism, University of Minnesota, Minneapolis, MN, USA, [5]Stanford Nano Shared Facilities, Stanford University, Stanford, CA, USA, [6]Department of Physics, Kaunas University of Technology, Kaunas, Lithuania

Key Points:

- Mixtures of multidomain to single domain Fe–Ni grains are the main magnetic carriers in Apollo mare basalts; magnetite is not present
- Lunar diurnal temperature cycling does not demagnetize mare basalts enough to affect standard paleointensity calculations
- High coercivity Fe–Ni grains within lunar mare basalts permit retention of ancient field records, such as from a dynamo

Supporting Information:

Supporting Information may be found in the online version of this article.

Correspondence to:

J.-I. Jung,
jiinjung@stanford.edu

Citation:

Jung, J.-I., Tikoo, S. M., Váci, Z., Krawczynski, M. J., Solheid, P., Burns, D. H., & Vailionis, A. (2025). Magnetic mineralogy in lunar mare basalts and implications for paleointensity retrieval. *Journal of Geophysical Research: Planets*, *130*, e2025JE009030. https://doi.org/10.1029/2025JE009030

Received 24 FEB 2025
Accepted 7 AUG 2025

Abstract Lunar paleomagnetic studies have identified multidomain metallic Fe–Ni alloys as the dominant magnetic contributors in mare basalts. Here, we explore the low-temperature magnetic behavior of standard samples for a suite of opaque minerals that occur within mare basalts (single-domain and multidomain Fe, wüstite, ulvöspinel, iron chromite, ilmenite, and troilite). We compare the observed low-temperature behaviors to those of several Apollo mare basalt samples (10003, 10044, 10020, 10069, 10071, 12009, 12022, 15597). Notable magnetic transitions were detected at <30 K (ilmenite), 60–80 K (chromite, troilite), and 100–125 K (ulvöspinel, chromite). We also investigated the effects of low-temperature cycling on mare basalt remanence and observed that only grains with coercivities <20–40 mT were cleaned. This suggests a minimal impact of diurnal temperature cycling at the lunar surface on the retrieved lunar paleointensity values. Using comprehensive electron microscopy techniques, including scanning electron microscopy (SEM), energy dispersive spectroscopy (EDS), wavelength dispersive spectroscopy (WDS), x-ray diffraction, and transmission electron microscopy (TEM), we further examined magnetic phases within four Apollo 11 mare basalt samples. Our findings revealed the presence of Fe grains (one to 10 μm in diameter) associated with troilite contain subgrains ranging in size from tens to hundreds of nanometers in some samples. These grains, which fall within the single-domain to multi-domain range as observed in their first-order reversal curves, might have the potential to retain high coercivity components and thereby effectively record an ancient dynamo field.

Plain Language Summary Scientists have been interested in the origin of magnetism recorded in the volcanic rocks brought back from the Moon during the Apollo and Chang'e missions. Originally, iron grains were believed to be the primary carriers, but two questions remained. First, the iron grains observed may be too large to effectively retain magnetic information. Second, previous studies investigating the low-temperature magnetic behavior of lunar volcanic rocks suggested that the mineral magnetite might also be present; if true, this would raise the possibility that rocks acquired magnetization during impact events long after their formation. Here, we conducted detailed rock magnetic experiments and microscopy analyses to reexamine the magnetic minerals in lunar volcanic rocks. Our results revealed two important findings: (a) We discovered very small, <100 nm particles of iron that are well suited for recording magnetic signals. (b) Contrary to earlier suggestions, we found no evidence of magnetite. Instead, the low-temperature behavior is explained by the mineral ulvöspinel. Additional low-temperature experiments revealed that temperature fluctuations at the lunar surface due to day/night cycles are unlikely to significantly alter the magnetism recorded. Overall, these findings suggest that Moon rocks contain minerals capable of preserving a stable record of the Moon's original magnetic field.

1. Introduction

Lunar mare basalts are a primary target lithology for investigating the history of the ancient lunar dynamo (Cai et al., 2024; Cournède et al., 2012; Jung et al., 2024; Shea et al., 2012; Suavet et al., 2013; Tarduno et al., 2021; Tikoo et al., 2012, 2014; Zhou et al., 2024). These basalts formed in a reducing environment and thus contain metallic Fe–Ni (or Fe–Ni–Co) alloys as primary magnetic remanence carriers (Tikoo & Evans, 2022; Weiss & Tikoo, 2014; Wieczorek et al., 2023). Previous magnetic hysteresis measurements suggest that these Fe–Ni grains fall within the multidomain (MD) grain size range (Cournède et al., 2012; Fuller, 1974; Strauss et al., 2021). In

addition, electron microscopy studies often observe Fe–Ni grain sizes ranging in diameter from approximately 1 to 100 μm; this size range is consistent with expectations for MD iron (Muxworthy & Williams, 2015).

Despite their MD nature (unstable domain stability and typically having low coercivity (LC) components), some samples exhibit stable high coercivity (HC) natural remanent magnetization (NRM) during alternating field (AF) demagnetization, indicating grain populations with good magnetic recording properties also exist within some mare basalts. Numerous studies interpret such samples to have captured records of a lunar dynamo during a high-field epoch (HFE) during the period prior to 3.5 Ga (Cournède et al., 2012; Jung et al., 2024; Nichols et al., 2021; Shea et al., 2012; Suavet et al., 2013). In contrast, samples formed after this HFE appear to have formed in weaker (∼5 μT) to null ambient magnetic fields (Cai et al., 2024; Strauss et al., 2021; Tikoo et al., 2014, 2017). We note that some HFE-aged mare basalts do not appear to contain records of dynamo fields (Cottrell et al., 2024; Cournède et al., 2012; Jung et al., 2024; Tarduno et al., 2021; Zhou et al., 2024). These seemingly contradictory findings raise important questions about why some MD Fe–Ni alloy-bearing samples contain stable HC remanence whereas others do not.

Although iron oxides are typically unexpected because of the Moon's restrictive redox conditions (Tikoo & Evans, 2022; Wadhwa, 2008), Apollo-era studies have suggested their presence as potential magnetic carriers in lunar materials (Forester et al., 1973; Jedwab et al., 1970; Runcorn et al., 1971). More recently, it has been identified in Apollo 16 regolith breccias as micrometer-scale disseminated domains within troilite, implying that variations in oxygen fugacity may occur (Joy et al., 2015). Nanometer-scale magnetite has also been observed in lunar soils collected by the Chang'e-5 mission, coexisting with troilite and metallic Fe, suggesting a eutectoid reaction under locally oxidizing conditions that likely resulted from impacts (Guo et al., 2022). More recently, a significant number of submicron magnetite grains have been further observed in lunar impact glass, with abundances positively correlated with the TiO_2 content of the surrounding glass (Cao et al., 2024), and hematite has also been proposed to exist at high latitudes (Li et al., 2020). These studies collectively indicate that iron oxides cannot be entirely ruled out as magnetic carriers. Interestingly, an Apollo-era paleomagnetic study also reported the potential identification of magnetite in mare basalts by observing a low-temperature (LT) magnetic transition at approximately 120 K that was interpreted as the Verwey transition (Runcorn et al., 1971). However, this finding was not widely pursued, as magnetite had not yet been identified by petrologists in mare basalt (Fuller, 1974). It was also suggested that the observed LT magnetic behavior could be attributed to chromite (Banerjee, 1972), which led to a lack of further search for iron oxides in lunar mare basalt over the last few decades.

In this study, we conducted comprehensive rock magnetic experiments, including LT behavior analysis using the Magnetic Properties Measurement System (MPMS) and first-order reversal curves (FORC) analysis, on selected Apollo mare basalt samples (10003, 10044, 10020, 10069, 10071, 12009, 12022, 15597), as well as standard minerals (single domain (SD) and MD Fe, wüstite, ulvöspinel, iron chromite, ilmenite, and troilite). In addition to exploring the low-temperature rock magnetic properties of mare basalts, we also investigated the effects of low-temperature cycling on remanent magnetization and paleointensity values of mare basalts. Finally, we used a range of electron microscopy techniques, including scanning electron microscopy (SEM), energy dispersive spectroscopy (EDS), wavelength dispersive spectroscopy (WDS), x-ray diffraction, and transmission electron microscopy (TEM) to examine the morphologies and occurrences of Fe grains in our mare basalt samples.

2. Low-Temperature Magnetic Properties of Minerals in Lunar Rocks

2.1. Background

LT magnetic behaviors (<300 K) allow the identification of magnetic mineralogy in terrestrial and extraterrestrial rocks, as several minerals exhibit clear magnetic transitions at these temperatures. Notable examples include the Verwey transition of magnetite at 120 K (T_V), the Morin transition of hematite at 262 K, and the Besnus transition of pyrrhotite at 32 K (Besnus & Meyer, 1964; Fillion & Rochette, 1988; Morin, 1950; Nagata et al., 1964; Verwey & Haayman, 1941). Given the reducing environment on the Moon, oxidized forms of iron $\left(Fe^{3+}\right)$ are expected to be absent, resulting in the LT magnetic signature being predominantly influenced by metallic Fe rather than iron oxides (Haggerty, 1978; Tikoo & Evans, 2022). It may be possible to detect other opaques, such as ilmenite, troilite, or spinel groups such as chromite and ulvöspinel, due to the presence of known LT magnetic transitions in these phases. Despite recent paleomagnetic and rock magnetic investigations on lunar mare basalts, detailed

studies on their LT magnetic remain lacking, even though some early Apollo-era studies exploring LT behavior in lunar materials (Nagata et al., 1970; Runcorn et al., 1971; Senftle et al., 1975). In this section, we describe the opaque minerals identified in various lunar mare basalt samples and their magnetic behavior under LT conditions. A brief overview of the interpretation of LT magnetic behavior is provided in Text S1; Table S1; Figure S1 of Supporting Information S1.

2.1.1. Metallic Fe

In lunar mare basalts, the low oxygen partial pressure during the original crystallization of lunar magma leads to the occurrence of native Fe in lunar rocks (Papike et al., 1991; Wieczorek et al., 2023). These metallic phases typically manifest as body-centered cubic Fe–Ni alloys (or sometimes Fe–Ni–Co alloys), including kamacite ($\alpha - Fe_{1-x}Ni_x$ for $x < \sim 0.05$) and martensite ($\alpha 2 - Fe_{1-x}Ni_x$ for $\sim 0.05 < x < \sim 0.25$), with T_C ranging from 770°C for pure Fe to below 660°C as Ni content increases (Liu et al., 2019; Wei et al., 2014). The composition of these metallic phases varies not only between samples but also within individual samples and across different lunar sites (Figure S2 in Supporting Information S1). The early formed olivine crystals can enclose native Fe with up to 30% Ni content, forming martensite (commonly observed in Apollo 12 and 15 basalts), while the Fe content in later-crystallized portions of the rock can be nearly pure metallic Fe, forming kamacite (commonly observed in Apollo 11 and 17 basalts) (Papike et al., 1991). These Fe–Ni grains are often associated with the troilite phase (FeS) as part of a eutectic assemblage (Skinner, 1970) or with chromium-ulvöspinel (Cr-rich spinel) or titanian-chromite (Ti-rich chromite) (Cameron, 1970; Gibb et al., 1970). They can be found in various forms, including interstitial grains, isolated within mesostasis glass, or as inclusions within silicates (Tikoo et al., 2014, 2017). These Fe–Ni alloys are considered to be the primary magnetic carriers in lunar mare basalts, likely within the MD regime (typically >1 μm in size) (Muxworthy & Williams, 2015).

2.1.2. Spinels

The spinel group is characterized by the general formula AB_2X_4, typically within a cubic crystal system. In this structure, cations A and B occupy the octahedral and tetrahedral sites, respectively, while X represents anions, usually oxygen. Magnetite (Fe_3O_4 or $Fe^{3+}\left[Fe^{3+}, Fe^{2+}\right]O_4$), a common magnetic carrier in terrestrial rocks, exhibits an inverse spinel structure. In magnetite, A sites $\left(Fe^{3+}\right)$ and B sites $\left(Fe^{3+}Fe^{2+}\right)$ are occupied by iron ions in different valences. Magnetite is notable for its T_V around 120 K, where it transitions from a cubic inverse spinel to a monoclinic structure (Verwey & Haayman, 1941; Walz, 2002). Recent studies have observed micrometer-scale magnetite in lunar regolith breccia 60016 (Joy et al., 2015) and submicroscopic magnetite in Chang'e-5 lunar soils and metallic Fe (Cao et al., 2024; Guo et al., 2022), magnetite has not, to our knowledge, been documented in lunar basalts.

However, other varieties of spinels are prevalent in mare basalts, making up to 10% of the basalts, particularly evident in samples from Apollo missions 12, 15, and 17 (Papike et al., 1991). These spinels exhibit a diverse range of compositions, including complex solid solutions such as ulvöspinel (Fe_2TiO_4), chromite ($FeCr_2O_4$), hercynite ($FeAl_2O_4$), and spinel ($MgAl_2O_4$), often represented in the Johnston compositional prism (Haggerty, 1971; Papike et al., 1991). Most lunar basalt spinel compositions fall between ulvöspinel and chromite as titanian chromites and chromian ulvöspinels $\left(Fe^{2+}_{1+n}Cr^{3+}_{2-2n}Ti^{4+}_{n}O_4\right)$ (Banerjee, 1972; Papike et al., 1991).

2.1.3. Spinel-Ulvöspinel

Ulvöspinel or titanium ferrite ($TiFe_2O_4$) has a inverse spinel structure, with Fe^{2+} occupying the A sites and a combination of Fe^{2+} and Ti^{4+} occupying the B sites. In terrestrial rock magnetism, ulvöspinel forms a solid solution with magnetite, $Fe^{2+}\left[Fe^{2+}_{(1-n)}Ti^{4+}_{n}\right]_2O_4$, where $0 < n < 1$ represents the molar fraction of Ti. Since Ti^{4+} does not have unpaired spins, the net magnetic moment is zero, and pure ulvöspinel ($n = 1$) exhibits antiferromagnetic behavior (Tauxe, 2008). However, the non-equivalence of the A and B sites, weak ferrimagnetism may be observed below 115 K (Ishikawa, 1967; Ishikawa et al., 1971; Readman, 1978).

2.1.4. Spinel-Chromite

Iron chromite ($FeCr_2O_4$) has a normal cubic spinel structure, where A and B sites are filled by Fe^{2+} and Cr^{3+}, respectively. Similar to the titanomagnetite solid solution, the Fe–Cr system can be expressed as

$Fe^{2+}\left[Fe^{3+}_{(1-n)}Cr^{3+}_{n}\right]_2 O_4$, where $0 < n < 1$ denotes the molar fraction of Cr. Pure iron chromite is ferrimagnetic, with a T_C typically between 70 and 80 K. However, T_C can vary up to 140 K depending on the molar fraction of Cr (from $n = 1$ to $n = 0.75$) (Hodel et al., 2020; Robbins et al., 1971). The low-temperature magnetic transition of chromite was identified at 90 K in the Martian meteorite ALH84001 (Antretter et al., 2003; Weiss et al., 2004), at 100 K in Apollo lunar basalt 12063, and between 40 and 80 K in ordinary chondrites, likely due to elemental substitutions such as Al, Mg, and other cations (Gattacceca et al., 2011).

2.1.5. Troilite

Troilite (FeS) is an iron sulfide and the most common sulfide mineral found in lunar mare basalts (Papike et al., 1991). Typically, troilite appears as interstitial, rounded anhedral grains, often containing small metallic Fe inclusions, and this structure is believed to have formed from a sulfide liquid that evolved from the silicate melt late in the crystallization sequence (Reid et al., 1970; Skinner, 1970). However, obtaining reliable paleointensity measurements from this mineral assemblage through heating methods is known to be challenging due to severe thermal alteration, particularly from interactions between these two minerals around 300–325°C (Chowdhary et al., 1987; Pearce et al., 1976). This temperature range corresponds to their T_N of approximately 588 K, up to which it remains antiferromagnetic. LT magnetic transitions around 70 K have been reported in troilite samples from the Bruderheim L6 chondrite and in troilite extracted from the Cape York IIIAB meteorite, possibly due to canting of the antiparallel spins or transition to ferromagnetic or ferrimagnetic (Cuda et al., 2011; Kohout et al., 2007). However, it has also been suggested that this transition might be attributed to the presence of chromite in ordinary chondrites instead of troilite (Gattacceca et al., 2011).

2.1.6. Ilmenite

Ilmenite ($FeTiO_3$) is a titanium-iron oxide mineral with a hexagonal crystal structure, consisting of alternating layers of titanium and iron-containing octahedra. It is the most abundant oxide mineral in lunar mare basalts (can make up as much as 15–20% by volume of many Apollo 11 and 17 mare basalts), with its concentration in these rocks being directly related to the titanium dioxide TiO_2 content of the original magma (Papike et al., 1991). In lunar ilmenite, some Mg substitutes for Fe, forming a solid solution between $FeTiO_3$ and $MgTiO_3$ (geikielite, a paramagnetic mineral). Ilmenite exhibits paramagnetic behavior at room temperature but transitions to an antiferromagnetic state at temperatures below its T_N, which ranges from 40 to 80 K. As ilmenite is cooled further, it transitions into a re-entrant spin-glass (RSG) phase below T_R, the temperature at which the change from RSG to antiferromagnetic occurs, spanning between 19 and 40 K (Burton et al., 2008; Engelmann et al., 2010; Senftle et al., 1975).

2.1.7. Wüstite

Wüstite (FeO) is an iron oxide (II) that crystallizes in a cubic structure similar to that of sodium chloride ($NaCl$). It is commonly found in meteorites, particularly in association with fusion crusts, where it forms through the oxidation or desulfurization of troilite (Horstmann et al., 2013). Although wüstite has not been directly observed in lunar rocks, the redox conditions governed by the iron-wüstite buffer on the Moon suggest that the lunar environment is capable of forming wüstite under specific conditions (Tikoo & Evans, 2022). Additionally, it has been proposed that the magnetite observed in lunar soils may result from the decomposition of wüstite (Guo et al., 2022). Wüstite has paramagnetic behavior at room temperature, but it transitions to an antiferromagnetic state below T_N around 200 K (Cornell & Schwertmann, 2003; McCammon, 1992).

2.2. Samples and Magnetic Methods

2.2.1. Samples

We collected various magnetic mineral standards that may be present in lunar mare basalts: SD to MD metallic iron (Fe), wüstite (FeO), ulvöspinel (Fe_2TiO_4), ilmenite ($FeTiO_3$), iron chromite ($FeCr_2O_4$) and troilites (FeS). Descriptions and sources for standard samples are tabulated in (Table 1; Text S2; Figure S3; Table S2 in Supporting Information S1). We also investigated nine Apollo mare basalts with various lithologies: three Apollo 11

Table 1
Standard Samples, Their Analog Target, Sample Types, Composition, and Sources

Sample ID	Standard analog	Types	Composition	Source/Manufacturer
STD-FE-SD	SD Iron (Fe)	Powder, (<25 nm)	Fe 99.9% based on trace metal basis	SkySpring Nanomaterials Product No: 0915SJ
STD-FE-MD	MD Iron (Fe)	Powder, (<10 μm)	Fe >99.5% based on trace metal basis	Alfa Aesar CAS No: 7439-89-6
STD-FE-MIX	SD + MD Iron (Fe)	Powder, (<25 nm-10 μm)	mixture of 50% of STD-FE-SD and 50% of STD-FE-MD	Mixture of STD-FE-SD STD-FE-MD
STD-WUS	Wüstite (FeO)	Powder, (<2 mm, 10 mesh)	FeO >99.6% based on trace metal basis	Sigma-Aldrich CAS No: 1345-25-1
STD-ULVO	Ulvöspinel (Fe_2TiO_4)	Chip (<50 μm)	76.7% Ulvöspinel, 23.3% of Ilmenite based on the estimation of abundances using k-mean clustering on SEM images	Synthesized by sintering FeO and TiO_2 see Text S1 in Supporting Information S1
STD-CHR	Chromite ($FeCr_2O_4$)	Powder (<100 μm)	Chromite See Figure S1, Table S1 in Supporting Information S1	Synthesized using FeO and Cr_2O_3 oxides see Text S1 in Supporting Information S1
STD-ILM	Ilmenite ($FeTiO_3$)	Chip	54.98 wt.% Geikielite, 40.56 wt.% Ilmenite, 4.46 wt. % hematite, (Liang et al., 2024)	Chipping from Kimberlite ilmenite megacryst Kumgbo, Liberia
STD-TRO-A	Troilite (FeS)	Chip	Troilite See Figure S1, Table S1 in Supporting Information S1	Diamond wire saw cutting from iron meteorite Muonionalusta, Sweden
STD-TRO-B	Troilite (FeS)	Chip	Troilite Iron Oxides veins See Figure S1, Table S1 in Supporting Information S1	Diamond wire saw cutting from iron meteorite troilite nodules

Note. SEM images and quantitative electron dispersive spectroscopy (Figure S3, Table S2 in Supporting Information S1); Note that a trace metal basis indicates the purity of the metal. Non-metallic phases or metal oxides (if the material has been exposed to air) may still be present. The process of synthesizing chromite and ulvöspinel is detailed in Text S2 of Supporting Information S1.

low-K ilmenite basalts (10003, 10020, 10044), two Apollo 11 high-K ilmenite basalts (10069, 10071), two Apollo 12 olivine basalts (12008, 12009), one Apollo 12 ilmenite basalt (12022), and one Apollo 15 pigeonite basalt (15597).

2.2.2. MPMS

Magnetic remanence measurements for each specimen were conducted at low temperatures using the Quantum Design third-generation magnetic property measurement system (MPMS) at the Institute for Rock Magnetism at the University of Minnesota. We measured field-cooled magnetization (FC), zero-field cooled magnetization (ZFC), room-temperature saturated isothermal remanent magnetization (RTsIRM), AC susceptibility measurements, and magnetization in field (J-T) curve. Our methodology strictly followed the Institute for Rock Magnetism standard protocol (Bilardello & Jackson, 2013) (Text S3; Figure S4 in Supporting Information S1). Detailed measurements for each sample are listed in (Table S3 in Supporting Information S1).

2.2.3. Magnetic Hysteresis and First-Order Reversal Curves

To better understand the coercivity distribution and the degree of magnetostatic interactions within our samples, we conducted magnetic hysteresis loop, backfield remanence, and room temperature first-order reversal curves (FORCs) analyses using a Lake Shore's vibrating sample magnetometer (VSM) at the IRM. Hysteresis curves were collected with a maximum applied field of 1.5 T with a field increment of 1 mT at room temperature. Then, the backfield remanence data were acquired with an initial field, field increment, and averaging time of 1.5 T, 1 mT, and 0.1 s, respectively. The measurement procedure for a single FORC involves (a) saturating the sample in a 1.5 T field, (b) decreasing the field to the reversal point (Ba) with an interval of 2 mT, and then (c) measuring M as a function of increasing field (Bb). This process is repeated for decreasing values of Ha from 100 to −100 mT, and 268 sets of FORCs were assembled. For standards, we conducted one FORC experiment. However, for all Apollo samples, the FORC protocol was repeated five times and measurements were stacked to reduce background noise. After data acquisition, hysteresis loops and backfield remanence data were processed using the IRM database software (Jackson & Solheid, 2010). IRM unmixing was applied to the IRM acquisition curves derived from backfield remanence curves, and their magnetic coercivity distributions were unmixed using

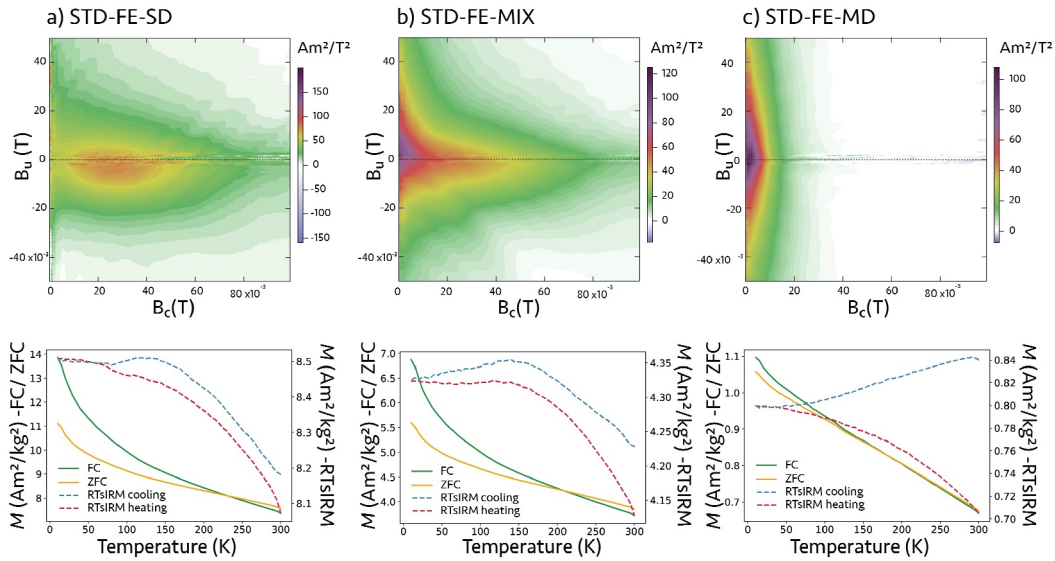

Figure 1. FORC diagrams and MPMS measurement for metallic Fe standard samples: (a) STD-FE-SD, (b) STD-FE-MIX, (c) STD-FE-MD. The top panels show FORCs distribution.

MaxUnmix online tool (Maxbauer et al., 2016). The FORC distribution was calculated as the mixed second derivative and analyzed using FORCinel software (Harrison & Feinberg, 2008).

2.3. Results: Standards

2.3.1. Standard: Metallic Fe

FORC diagrams for our spherical iron powder samples demonstrate distinct magnetic domain characteristics (top panels in (Figure 1), see hysteresis loops in (Figure S5 in Supporting Information S1)). Our STD-FE-SD (iron powder samples with diameters less than 25 nm) exhibit interacting SD features, indicated by a broad central ridge in the FORC diagram. In contrast, STD-FE-MD (iron powder samples with diameters less than 10 μm) display clear MD features, including a vertical distribution along the Bu axis. The STD-FE-MIX samples, which contain mixtures of these particle sizes in equal ratios, reveal both SD and MD features, affirming the presence of both grain types. The coercivity ranges obtained from the IRM unmixing for STD-FE-SD, STD-FE-MD and STD-FE-MIX were 37.25–64.07 mT, 6.97–28.54 mT, and 32.51–59.67 mT, respectively (Figure S6; Table S4 in Supporting Information S1).

MPMS results for Fe samples of STD-FE-SD, STD-FE-MIX, and STD-FE-MD present some notable observations (bottom panels in (Figure 1)). As the temperature increases, FC and ZFC magnetizations decrease. A crossing of the ZFC and FC curves is observed between 150 and 250 K for all samples; this is also observed in Fe–Ni alloy samples by Kohout et al. (2007). This characteristic possibly indicates the presence of multiple domain states or grain sizes (Smirnov, 2009). Another significant observation is the greater difference between the FC and ZFC curves at lower temperatures for the SD iron samples $\left([M_{ZFC}/M_{FC}]_{T=10K} = 77.39\%\right)$ compared to the MD samples $\left([M_{ZFC}/M_{FC}]_{T=10K} = 92.69\%\right)$. This suggests a marked increase in susceptibility for SD grains at low temperatures, potentially indicating a superparamagnetic signature. One explanation is that a larger number of free magnetic spins on the surface of SD particles, compared to MD particles, contributes to this effect. Additionally, RTsIRM measurements show more pronounced separation at higher temperatures in MD samples, suggesting that domain rearrangements during heating and cooling cycles contribute to some degree of demagnetization (Halgedahl & Jarrard, 1995). Since the samples were not subjected to low-temperature experiments in a reducing environment, the weak Verwey transition in RTsIRM curves may indicate partial oxidation during the measurements on these powdered samples.

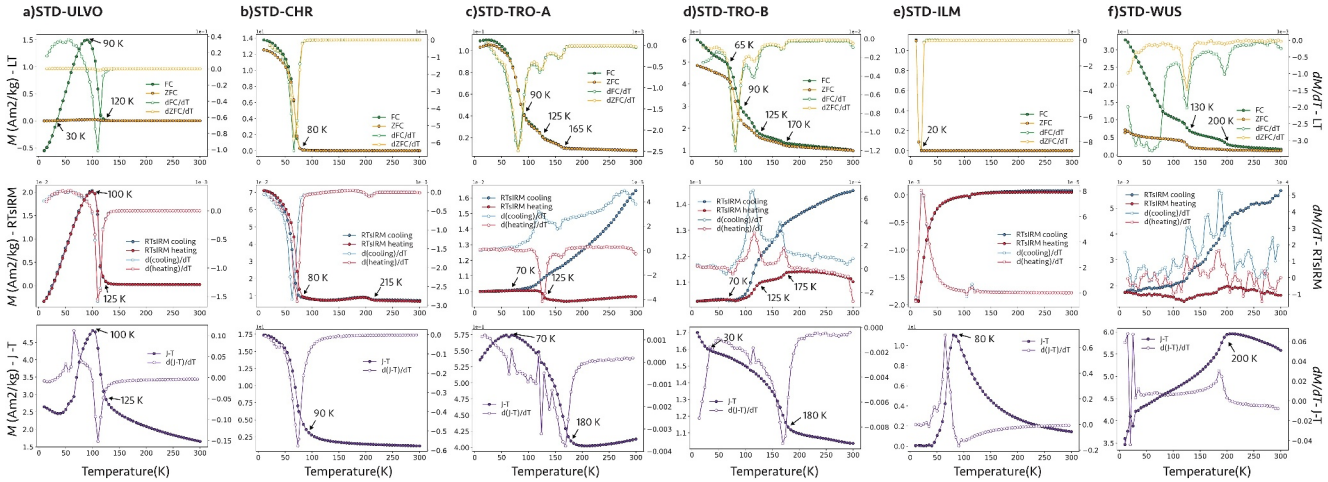

Figure 2. MPMS measurements for synthetic ulvöspinel. (a) STD-ULVO, iron chromite. (b) STD-CHR, troilite samples from iron meteorite. (c) STD-TRO-A and (d) STD-TRO-B, ilmenite chip. (e) STD-ILM, and wustite powder. (f) STD-WUS. The top panels display the FC and ZFC curves, the middle panels show the RTsIRM cooling and heating curves, and the bottom panels present the J-T curves. Open circles indicate the derivatives of these curves.

2.3.2. Standard: Ulvöspinel

Our LT curves for synthetic ulvöspinel (STD-ULVO) do not reveal purely antiferromagnetic behavior but exhibit some remanence at LT. We observed peak magnetic moments at 90–100 K, followed by a decline at 120–125 K, corresponding to a T_C (or T_N depending on whether the remanence is interpreted as slight ferrimagnetic behavior) (Figure 2a). The peak magnetic susceptibility occurs at 110 K, and it also shows frequency dependencies around this temperature (Figure S7 in Supporting Information S1). Beyond this temperature range, the material exhibits paramagnetic behavior (see pure paramagnetic behavior in the magnetic hysteresis loop at room temperature (Figure S5 in Supporting Information S1)), consistent with previously reported synthesized polycrystalline $0.95Fe_2TiO_4$ (Readman, 1978). Note that the subtle remanence from the IRM unmixing curve could potentially be magnetic remanence from submicron interstitial melts (Figures S3 and S6 in Supporting Information S1). The observed remanence can be attributed to a spontaneous local distortion of the crystal structure at low temperatures, such as the Jahn-Teller effect (Nakamura & Fuwa, 2014). This could also indicate an imbalance in sublattice moments, suggesting ferrimagnetic behavior. In this case, the FC and RTsIRM curves show a Néel N-type thermomagnetic curve with a compensation point at 30 K (pure antiferromagnetic behavior), a characteristic similar to that observed at 40 K, reflecting the intrinsic properties of ulvöspinel (Readman, 1978). This behavior indicates that at temperatures ranging from absolute zero up to 30 K, $M_B < M_A$, whereas at temperatures above 30 K, $M_B > M_A$. Our sample contains approximately 23% ilmenite (antiferromagnetic), which exhibits a slight signature around 60–80 K (T_N) in the J-T curve and susceptibility curves.

2.3.3. Standard: Chromite

Our FC, ZFC, RTsIRM, and J-T curves for synthetic iron chromite (STD-CHR) show a drop at around 80–90 K (T_C), followed by the transitioning to paramagnetic behavior (Figure 2b). The peak magnetic susceptibility occurs at 110 K, and it also shows frequency dependencies around this temperature (Figure S6 in Supporting Information S1). This T_C temperature range agrees with that reported for pure chromite by Robbins et al. (1971) and chromite found in ordinary chondrites (Gattacceca et al., 2011). The RTsIRM curves exhibit a subtle magnetic signature at 215 K, which may indicate a minor magnetic phase transition, possibly due to impurities or secondary mineral phases.

2.3.4. Standard: Troilite

Our troilite samples (STD-TRO-A and STD-TRO-B) exhibited magnetic transitions at approximately 70–90, 125, and 165 K (Figures 2c and 2d). The transition near 90 K may correspond to a known phase transition in troilite, as previously described (Cuda et al., 2011; Kohout et al., 2007), and is accompanied by a slight separation in the

Table 2
Summary of Magnetic Transition Temperatures and Behaviors Observed in Standard Samples

Sample ID	Analog	LT characteristics	FC	ZFC	RTsIRM	J-T	Note
STD-FE-SD	SD Iron	No Feature	–	–	–	–	FC ≫ ZFC, RTsIRM ↓
STD-FE-MIX	SD + MD Iron	No Feature	–	–	–	–	FC > ZFC, RTsIRM ↓↓
STD-FE-MD	MD Iron	No Feature	–	–	–	–	FC ~ ZFC, RTsIRM ↓↓↓
STD-WUS	Wüstite	190–200 K (T_N)	–	–	–	T_N	Impurities: 125–130 K
STD-ULVO	Ulvöspinel	30–40 K (T_{comp}), 100–125 K (T_N)	T_{comp}, T_C	T_{comp}, T_C	T_C	T_C	–
STD-CHR	Chromite	70–140 K (T_C)	T_C	T_C	T_C	T_C	Impurity 215 K
STD-ILM	Ilmenite	< 19–40 K (T_{RSG}), 60–80 K (T_N)	T_{RSG}	T_{RSG}	–	T_N	–
STD-TRO	Troilite	70–90 K (T_{trans})	T_{trans}	T_{trans}	T_{trans}	–	Impurity 125, 160–180 K

Note. Curie temperature (T_C), Néel temperature (T_N), compensation temperature in N-type ferrimagnetism (T_{comp}), potential re-entrant spin-glass transition temperature (T_{RSG}), and other magnetic transitions (T_{trans}) are indicated. The relative difference in magnetic moment between FC and ZFC curves at very low temperatures is expressed as: FC ≫ ZFC (large difference), FC > ZFC (moderate difference), and FC ~ ZFC (small difference). The symbol ↓ denotes the extent of RTsIRM moment decrease upon thermal cycling: ↓ (slight decrease), ↓↓ (moderate decrease), ↓↓↓ (significant decrease).

RTsIRM curves. While standard powder XRD confirms a strong match with the reference troilite pattern (PDF 04-005-5124) (Text S4; Figure S8 in Supporting Information S1), it does not conclusively rule out the presence of minor impurity phases, such as chromite or iron oxides, that may exist below the detection threshold (~2–5 wt.%). Therefore, the presence of trace impurity phases that may contribute to the observed 90 K transition cannot be entirely ruled out. The transitions at 125 and 165 K were observed but remain unidentified, as neither microscopy nor X-ray diffraction analyses allowed for definitive phase assignment. Room-temperature hysteresis measurements also reveal ferromagnetic behavior, suggesting that our troilite standards may not serve as an ideal pure standard (Figure S5 in Supporting Information S1). The STD-TRO-B sample features iron oxide veins, which may be linked to the magnetic transition detected between 165 and 180 K in the FC, ZFC, RTsIRM, J-T, and susceptibility measurements.

2.3.5. Standard: Ilmenite

Our ilmenite sample (STD-ILM) exhibits a clear antiferromagnetic behavior, with a significant magnetic transition occurring at 20 K in the FC, ZFC, and RTsIRM curves (Figure 2e, Figure S4 in Supporting Information S1). Our magnetic susceptibility curves also show a peak intensity at 20 K, with imaginary frequency dependent components observed below 50 K, possibly indicating an antiferromagnetic phase to the RSG state occurring (< 40 K) (Burton et al., 2008; Harrison, 2009). Consistent with previous studies, our sample also shows a clear T_N around 60–80 K in the J-T curve (Engelmann et al., 2010; Senftle et al., 1975).

2.3.6. Standard: Wüstite

We observed a clear magnetic transition at 200 K in the J-T curve (Figure 2f), which is consistent with the T_N of wüstite (Cornell & Schwertmann, 2003; McCammon, 1992). Slight transitions at this temperature were also observed in the FC, ZFC, RTsIRM curves. Another magnetic transition was detected at 125 K in the FC, ZFC, and RTsIRM curves, likely corresponding to the T_V of magnetite. This is not unexpected, as wüstite is unstable under the redox conditions present on Earth and tends to oxidize to more stable forms (particularly in powdered samples that may have oxidized upon exposure to air during measurements similar to Fe powders). Additionally, a further change was noted near 75 K, although the specifics of this transition remain unclear.

Comprehensive magnetic behaviors of our standard minerals, based on our results and previous studies, are summarized in Table 2, along with treatment conditions and representative FC, ZFC, and RTsIRM curves (see also (Figure S9 in Supporting Information S1)).

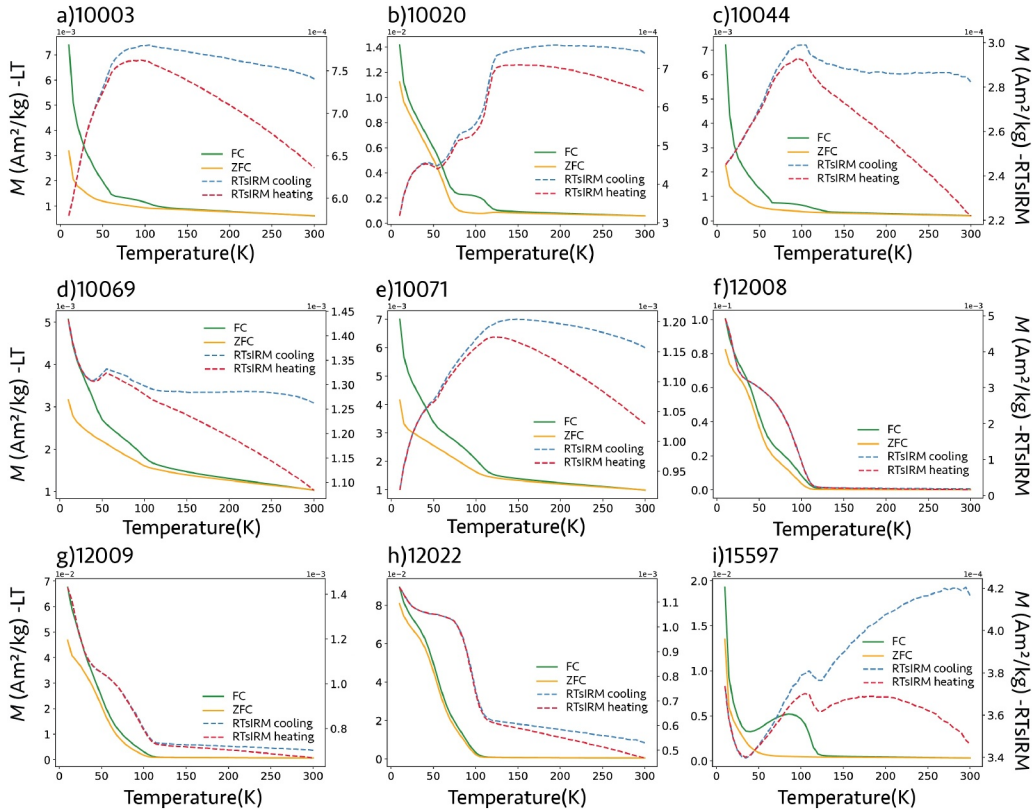

Figure 3. FC, ZFC, and RTsIRM curves for Apollo samples (a) 10003, (b) 10020, (c) 10044, (d) 10069, (e) 10071, (f) 12008, (g) 12009, (h) 12022, and (i)15597.

2.4. Results: Lunar Mare Basalts

2.4.1. MPMS

All Apollo samples exhibited a decrease in the FC and ZFC curves as the temperature increased, possibly due to the presence of metallic Fe (see Section 2.3.1) (Figure 3). A magnetic transition was observed in all samples at approximately 100–120 K in the FC and ZFC curves, which closely resembles the T_V of magnetite. However, given the absence of iron oxides in these samples by detailed microscopy (see Section 4), this comparison remains speculative. Instead, considering the magnetic transition of ulvöspinel at 120 K and chromite at >70 K (see Sections 2.3.2 and 2.3.3), we propose that the observed signature may be attributed to minerals from the ulvöspinel-chromite series, such as titanian chromite or chromium ulvöspinel. Some Apollo mare basalts in our samples were reported to contain chromite, ulvöspinel, or Cr-spinel (e.g., 10020 (Haggerty et al., 1970), 12008, 12009, 12022 (Neal et al., 1994), and 15597 (Weigand & Hollister, 1973)). Although ulvöspinel-chromite series minerals were not previously reported in Apollo samples 10003, 10044, 10069, and 10071, SEM and EDS analyses revealed a very small phase of ulvöspinel associated with ilmenite in samples 10003 and 10044 (see Section 5).

Another significant feature is the remanence transition observed around 60–80 K in the FC and RTsIRM curves. While this transition is consistent with the expected magnetic transition of troilite at 60–90 K (see Section 2.3.4), it is more likely dominated by the ulvöspinel-chromite series (the curve begins to drop drastically from 50 K, although iron chromite T_C is approximately >70 K (Figure 2b) or possible elemental substitutions), given troilite's weak magnetic signature (1–2 orders of magnitude lower than ulvöspinel/chromite) and low abundance in lunar mare basalts (<1%). The transition <40 K might be attributed to the T_{RSG} of ilmenite, while its T_N occurring near 60 K is distinctly captured in both the susceptibility measurements (Figure S10 in Supporting Information S1) and the J-T curves (Figure S11 in Supporting Information S1). Sample 15597 does not contain ilmenite and does not exhibit any susceptibility peak at 60 K.

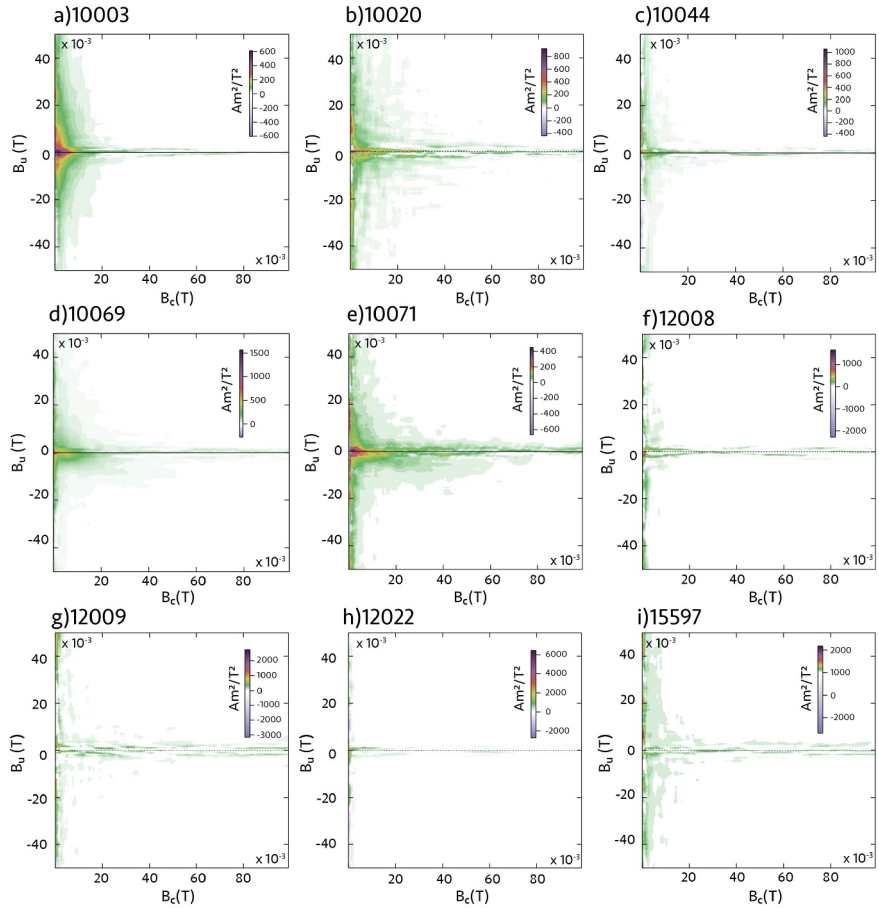

Figure 4. FORC diagram for Samples (a) 10003, (b) 10020, (c) 10044, (d) 10069, (e) 10071, (f) 12008, (g) 12009, (h) 12022, and (i)15597. The FORC diagram presents the mixed second derivatives of FORCs, indicating the relationship between magnetostatic interactions (B_u) and magnetic coercivity (B_c). The data presented is the result of compiling five separate FORC experiments for each sample ($N = 268$ FORCs). Analysis was performed using the FORCinel software package (Harrison & Feinberg, 2008).

The RTsIRM curves showed a reduction in magnetization of 5%–21% after cooling and heating, likely due to the MD behavior of Fe (as further supported by their magnetic hysteresis loops (Figure S12 in Supporting Information S1)). The effect of this demagnetization on lunar paleointensity was further investigated through mineral identification and analysis of their LT magnetic behavior (see Section 3). The non-zero, and nearly temperature independent of imaginary susceptibility is also likely due to self-demagnetization and weak-field hysteresis, as expected for these MD behaviors (Figure S10 in Supporting Information S1).

2.4.2. FORC

All samples exhibit a cluster at $B_c = 0$ that extends along the B_u axis, indicating the presence of MD and pseudo-single-domain-like grains (Figure 4), as can be observed in their hysteresis loops (Figure S12; Table S5 in Supporting Information S1). Samples 10003, 10020, 10069, 10071, and 15597 additionally show signatures of a horizontal ridge reaching high coercivity (>100 mT) along $B_u = 0$, which is consistent with the HC components observed in IRM unmixing results (Figure 5; Table S6 in Supporting Information S1). These features may indicate the presence of possible SD grains in the samples, such as nanometer-sized metallic Fe grains (Muxworthy & Williams, 2015) or other types of magnetic minerals that are too minute to be detected by petrographic microscopy. In contrast, samples 10044, 12008, 12009, and 12022 exhibit weak and noisy FORC diagrams, which aligns with their low magnetic grain abundances and their poor magnetic recording properties (Jung et al., 2024; Strauss et al., 2021; Tikoo et al., 2014).

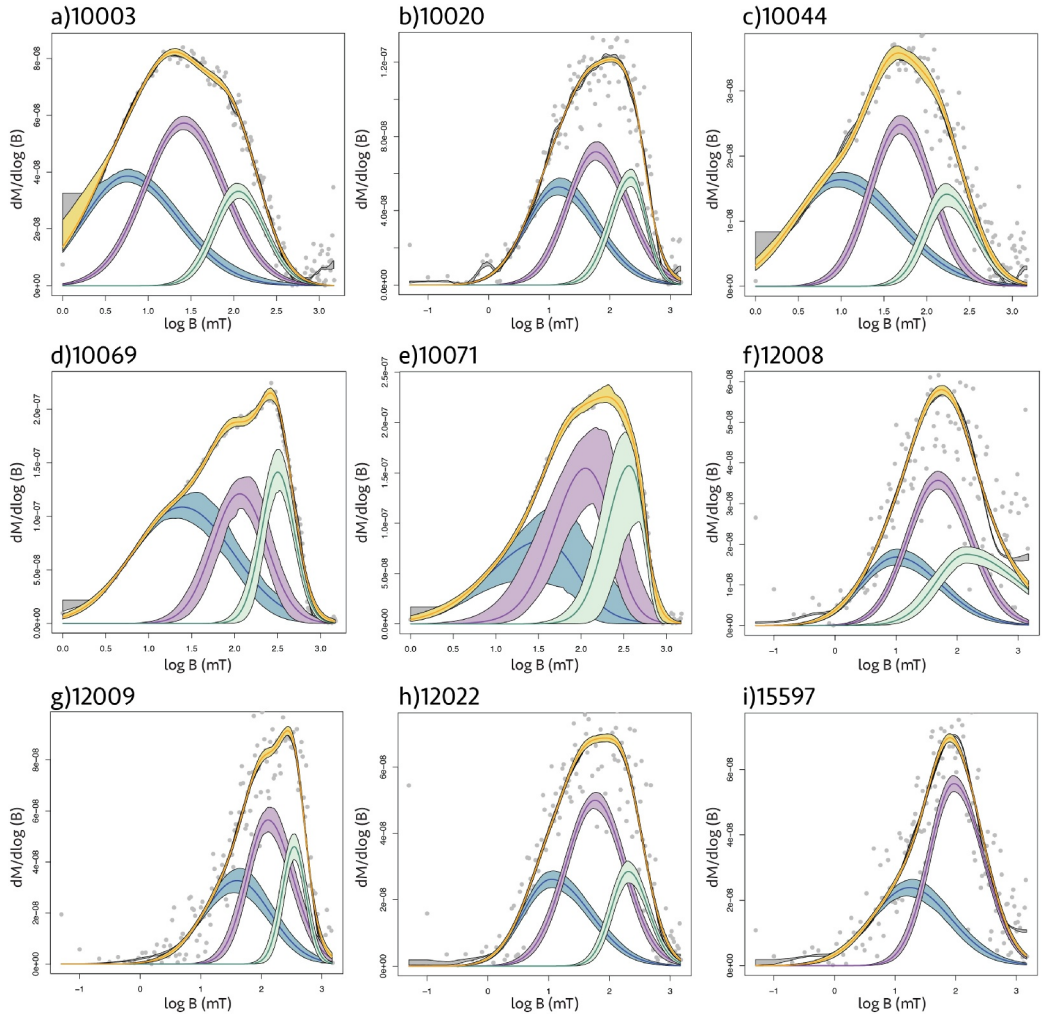

Figure 5. IRM unmixing results for samples (a) 10003, (b) 10020, (c) 10044, (d) 10069, (e) 10071, (f) 12008, (g) 12009, (h) 12022, and (i) 15597 obtained using the Maxunmix software. Gray circles illustrate actual data, while yellow curves depict the best-fit models. Different colors and shadings represent various coercivity components and the 95 % confidence intervals.

3. The Effect of Lunar Diurnal Temperature Fluctuations on Paleointensity Records

3.1. Background

The temperature at lunar landing sites (mainly on the equator ranging from 8.99°S to 26.10°N for the Apollo missions and 43.1°N and 41.64°S for Chang'e 5 and 6, respectively) fluctuates dramatically, reaching up to ∼397 K (∼124°C) during the day and plunging down to ∼95 K (−178°C) at night (Williams et al., 2017). Given that most lunar rocks contain MD Fe–Ni grains or potentially interacting SD grains (Jung et al., 2024; Weiss & Tikoo, 2014), such extreme temperature fluctuations can induce changes in magnetic moments due to domain-wall motion, reconstruction, or similar processes observed in magnetite (Dunlop, 2003; Halgedahl & Jarrard, 1995; Hodych et al., 1998; Yamamoto et al., 2003).

3.2. Experiments

Given our observation of a decreased RTsIRM under LT conditions, we aim to assess how lunar temperature fluctuations might influence paleointensity retrieval. To achieve this, we simulate the lunar thermal environment to quantify the extent of demagnetization from LT cycling. Our experimental approach consists of the following steps (Figure S13 in Supporting Information S1): First, we imparted a magnetization to the sample by applying a

Table 3
Magnetic Properties and Changes in Paleointensity Estimates of Selected Apollo Samples Following Low-Temperature Treatment

Sample	Lithology	Mass (mg)	NRM (Am^2/kg)	PI_{ARM}, PI_{sIRM}	$\delta_{ARM,0}$, $\delta_{sIRM,0}$	γ_{ARM}, γ_{sIRM}
10020, 259	Ilmenite Basalt	88.0	1.83e−5	121.80 ± 11.53 μT, 88.93 ± 5.45 μT	−5%, 13%	1.11 ± 0.04, 1.12 ± 0.01
12009, 156	Olivine Basalt	59.2	9.27e−7	1.56 ± 3.08 μT, 0.62 ± 1.15 μT	10%, 11%	0.76 ± 0.04, 1.09 ± 0.02
65035, 156	Impact Melt Glass	104.0	2.25e−4	8.87 ± 14.28 μT, 3.43 ± 5.49 μT	8%, 10%	0.96 ± 0.02, 1.06 ± 0.01

Note. The first, second, and third columns contain specimen names, lithologies, and masses, respectively. The fourth through seventh columns contain values for NRM, ARM, and sIRM paleointensity value, δ_{ARM}, δ_{sIRM}, γ_{ARM}, and γ_{sIRM}, respectively.

laboratory-induced magnetic field, serving as an analog for thermoremanent magnetization (TRM). Next, the sample is subjected to LT conditions to simulate lunar temperature cycling. Finally, we evaluate the degree of demagnetization and corresponding paleointensity changes following the LT treatment.

We conducted this test on three lunar samples with different lithologies and paleointensity values (Chaffee et al., 2023; Shea et al., 2012; Strauss et al., 2021): 10020 (ilmenite basalt), 12009 (olivine basalt), and 65035 (impact melt glass) (Table 3). First, we applied stepwise AF-demagnetization up to 100 mT. Next, samples were imparted with room-temperature anhysteretic remanent magnetization (ARM) as a TRM analog, using a dc bias field of 100 μT and an ac field of 200 mT, followed by stepwise AF demagnetization. We then re-applied ARM and placed the samples in liquid nitrogen ~77 K (~−195°C) for an hour within our magnetically shielded room. After cooling, the samples were allowed to warm back to room temperature inside the shielded room before undergoing another stepwise AF demagnetization. This step mimics exposure to cold conditions at lunar night in a null ambient magnetic field. We repeated the same procedure after imparting the samples with saturated isothermal remanent magnetization (sIRM) at a saturation field of 900 mT. These experimental protocols were executed using a 2G Enterprises 755 superconducting rock magnetometer (sensitivity limit $\sim 10^{-12} Am^2$) that is housed within a magnetically shielded room (ambient field <300 nT) at the Stanford Paleomagnetism Laboratory.

We followed non-heating paleointensity methods (i.e., ARM and IRM methods), using the following equations: $B_{anc} = f' \Delta NRM/\Delta ARM \times b$ and $B_{anc} = a\Delta NRM/\Delta sIRM$, where B_{anc} is the ancient magnetic field, b is the applied biased field, and ΔNRM, ΔARM, $\Delta sIRM$, represent the ancient magnetic field and the stepwise moment changes in NRM, ARM, sIRM, respectively. For our experiments, we used calibration factors of f' = 1.3 μT and a = 2,070 μT for the ARM and IRM methods, respectively (Weiss & Tikoo, 2014; Wieczorek et al., 2023). The change in magnetic moments after the LT exposure of samples (δ) is at each AF demagnetization step i is given by:

$$\delta_{ARM,i}(\%) = \frac{ARM_i - LTARM_i}{ARM_i} \times 100 \quad (1)$$

$$\delta_{sIRM,i}(\%) = \frac{sIRM_i - LTsIRM_i}{sIRM_i} \times 100 \quad (2)$$

where ARM_i and $sIRM_i$ are the magnetic moments of ARM and sIRM at AF demagnetization step i, while $LTARM_i$ and $LTsIRM_i$ indicate their respective magnetic moment after the LT treatments at the same AF step. To quantify the influence of LT exposure of samples to their ARM and IRM paleointensity, we also computed the paleointensity modification factor (γ) using the formula

$$\gamma_{ARM} = \frac{\Delta LTARM}{\Delta ARM} \quad (3)$$

$$\gamma_{sIRM} = \frac{\Delta LTsIRM}{\Delta sIRM} \quad (4)$$

where $\Delta LTARM$, $\Delta LTsIRM$ refer to the stepwise moment changes following an hour exposure to low temperatures. γ values close to 1 indicate minimal effects of low temperature cycling on retrieved paleointensity values.

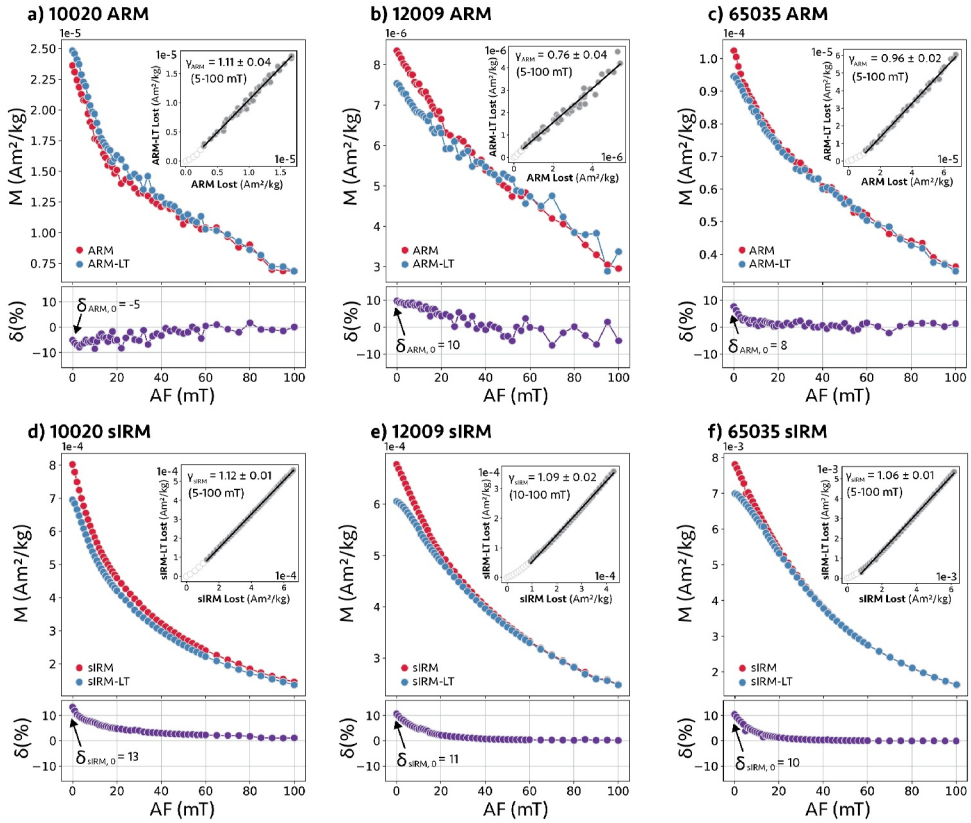

Figure 6. AF demagnetization curves for ARM before and after LT exposure (a–c) and sIRM before and after LT exposure (d–f). The bottom figures display the associated percent change in total moments (δ) following LT exposure. Insets within each graph show either ARM lost versus LT treated ARM lost or sIRM versus LT treated sIRM lost for the paleointensity modification factor (γ) calculations.

3.3. Results

The calculated ARM and sIRM paleointensity values for samples 10020, 12009, and 65035 are consistent with previously reported measurements (Chaffee et al., 2023; Shea et al., 2012; Strauss et al., 2021) (Table 3). Figure 6 presents AF demagnetization curves for ARM and sIRM before and after the LT treatment. The change in magnetization following LT treatment (δ) was minimal, with $\delta_{ARM,0}$ ranging from −5% to 13%, and $\delta_{sIRM,0}$ from 10% to 13%. These changes were limited to the lower coercivity fractions, as δ values approached zero with AF demagnetization levels of 20–40 mT. Given that γ_{ARM} ranged from 0.76 to 1.11 and γ_{sIRM} from 1.06 to 1.12, the low-temperature exposure would not alter the paleointensities retrieved from lunar samples by more than 25%.

4. Detailed Metallic Fe Microscopy

4.1. Methods

To examine the morphologies and occurrences of metallic Fe in our samples (10003; 10044; 10020; 10069; 10071; 12008; 12009; 12022; and 15597), we conducted comprehensive petrographic and compositional analyses using electron microscopy at the Stanford Scanning Electron Microscope Facility (SEMF) and Microchemical Analysis Facility (MAF). We performed backscatter scanning electron microscopy (BSEM) with EDS using a JEOL JSM-IT500HR environmental scanning electron microscope. WDS results for these samples have been previously reported in other works (Jung et al., 2024; Strauss et al., 2021; Tikoo et al., 2014) (Figure S2 in Supporting Information S1). In this study, we further performed WDS scans specifically on samples 10069 and 10071 to quantify elemental concentrations in Fe–Ni grains and to assess the potential presence of iron oxides. These scans were conducted at energy levels of 7 and 20 keV with a focused electron beam, using a consistent probe current of 20 nA. The scanning parameters included a working distance of 70–120 mm, a dwell time of

25–50 ms, and a step size of 10 μm, with an estimated spatial resolution of approximately 1–2 μm. Prior to WDS measurements, samples were polished using a 1 μm diamond polishing paste in order to remove any surface oxidation from the topmost layer.

In a continuation of the lunar TEM investigation presented in Jung et al. (2024), we applied focused ion beam (FIB) and TEM techniques on metallic Fe grains to obtain chemical and structural information at the nanometer scale. FIB sample extraction was performed on Fe grains associated with troilite in samples 10003,184, 10044,49, 10069,33, and 10071,31. Sample preparation involved applying platinum strips with a thickness of 2 μm followed by extraction and thinning with a STEM Thermo Fisher Scios 2 DualBeam FIB with a Ga ion source. The ion beam was operated at 30 kV with a current of 1–5 nA to extract sections, which were then further thinned using progressively lower currents at 30 kV, followed by cleaning steps at 16, 8, 5, and 2 kV. High-angle annular dark field (HAADF) and bright field (BF) imaging were conducted using a JEOL JEM-2100F Field-Emission STEM, with TEM Energy-dispersive X-ray (EDX) mapping and selected area electron diffraction (SAED) for in-depth structural and compositional analysis. All TEM analyses were performed at the Institute of Material Science and Engineering (IMSE) at Washington University in St. Louis.

4.2. Results

General petrographic observations are in agreement with the microtextural descriptions previously documented in the Lunar Sample Compendium. Samples 10003, 10044, and 12022 are ilmenite basalts exhibiting granular textures: 10003 is medium-grained, vuggy, and subophitic; 10044 is coarse-grained, vuggy, and ophitic; and 12022 is medium-grained and porphyritic. Samples 10020, 10069, and 10071 are ilmenite basalts displaying fine-grained textures: 10020 is fine-grained, vesicular, vuggy ophitic; 10069 is very fine-grained, vuggy to vesicular, and granular; and 10071 is fine-grained, vesicular to vuggy. Samples 12008 and 12009 are classified as olivine basalts with a porphyritic vitrophyre texture, which consists of skeletal phenocrysts, and sample 15597 as a pyroxene basalt with vitrophyric texture. We note that we do not find any petrographic evidence of shock in all the samples except 10044 (undulatory extinction of pyroxene grains indicative of shock >5 GPa). Modal mineral abundances determined in previous studies are compiled in (Table S7 in Supporting Information S1).

The primary silicate background minerals in all samples are pyroxene and plagioclase. Additionally, olivine ($Fo_{76–49}$) is present in samples 10020, 12008, 12009, and 12022, while mesostasis is also observed in samples 12008, 12009, and 15597 (Papike et al., 1991) (Figure 7). All samples contain Fe grains embedded in troilite as part of a eutectic assemblage (e.g., 10003, 10020, 10044, 10069, 10071, 12008, 12009, 12022) or in association with chromite-ulvöspinel series and silicates (e.g., 12008, 12009, 15597). WDS results indicate that the metallic Fe in these samples is predominantly kamacite (10003, 10020, 10044), martensite (12008, 12009), or a mixture of both (10069, 10071, 12022, 15597), with cobalt concentrations up to 2% in our samples (Jung et al., 2024; Strauss et al., 2021; Tikoo et al., 2017) (Figure S2 in Supporting Information S1).

The initial EDS mapping revealed the presence of oxygen traces in many Fe grains within the troilite phase of the samples (Figures S14–S18 in Supporting Information S1). WDS scans of the metallic phase in samples 10069 and 10071 also showed distinct peaks for Fe (Lα and Lβ) and oxygen (Kα), with oxygen concentrations ranging from 3 to 4 wt.%, while the standard metallic Fe samples analyzed in the same session did not show an oxygen peak (Figures S19b and S20–22 in Supporting Information S1). However, our TEM EDX analysis of these samples did not detect any significant oxygen content, and the SAED analysis mainly showed body-centered cubic metallic Fe (Figure S17f in Supporting Information S1). The presence of oxygen in our EDS and WDS scans likely resulted from surface oxidation from exposure to Earth's atmosphere, especially considering the age of the thin sections (~50 years), and sample polishing did not appear to effectively remove the surface oxidation.

TEM HAADF and BF imaging uncovered distinctive Fe grain textures in all samples (Figure 8). In sample 10003, single-crystal structures larger than 1 μm appear with some grain defects, potentially indicating low coercivity MD grains. Similarly, the FIB cross section of sample 10044 reveals two large Fe–Ni single-crystal grains (>1 μm) with some lattice distortions, also indicative of MD grains. However, samples 10069 and 10071 exhibit small and complex subgrain structures measuring 10–100 nm across, each with markedly different orientations. Several of these Fe subgrains may be associated with HC components (Jung et al., 2024), given that metallic Fe typically transitions from SD to MD state between 20 and 50 nm for spherical grains (Muxworthy & Williams, 2015). Non-spherical grains (e.g., elongated or oblate) can retain stable magnetization at larger sizes (a few 100 nm), as they may instead enter a single-vortex (SV) state before eventually transitioning to the MD state

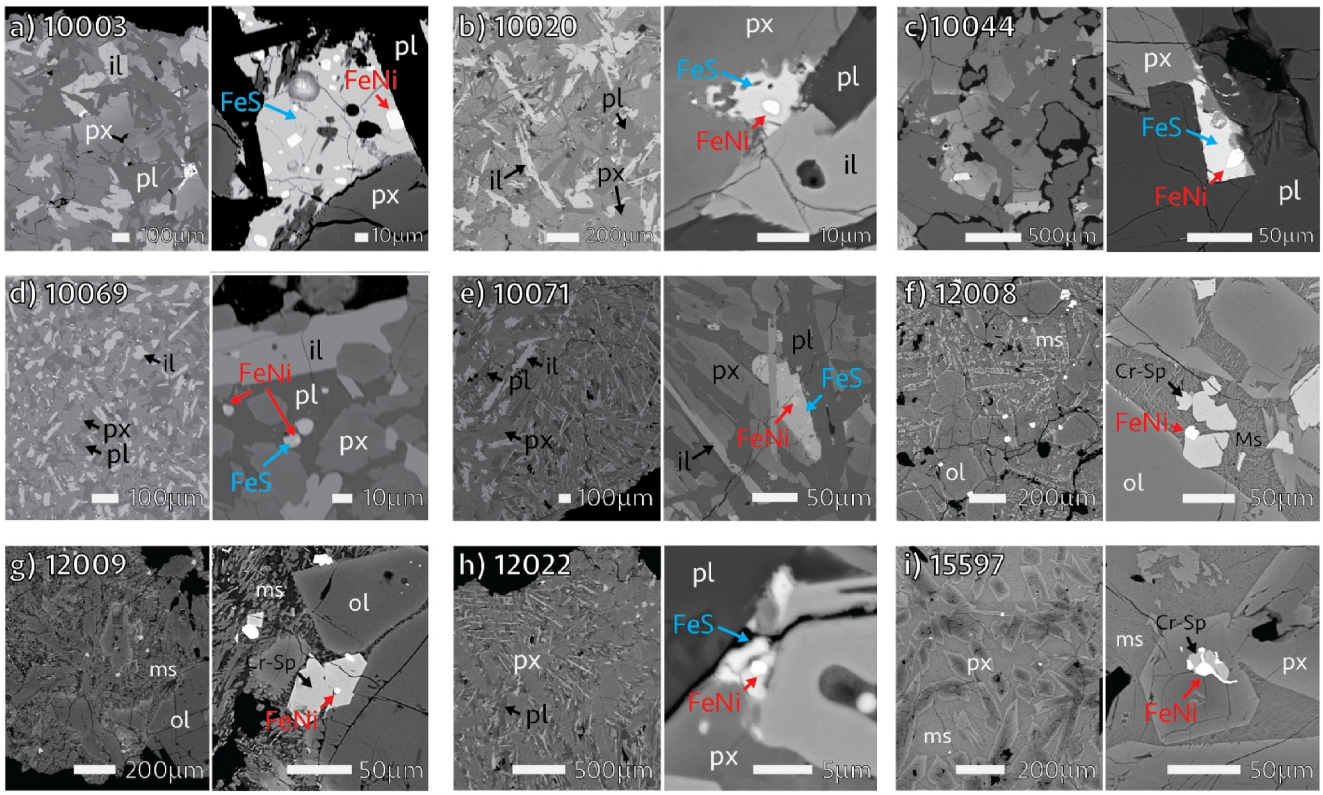

Figure 7. Electron microscopy investigation of Apollo mare basalts for samples: (a) 10003, (b) 10020, (c) 10044, (d) 10069, (e) 10071, (f) 12008, (g) 12009, (h) 12022, and (i) 15597. The images on the left are backscatter scanning electron microscopy (BSEM) images, providing an overview of the general mineralogical composition, prominently featuring plagioclase (pl), ilmenite (Ilm), and pyroxene (px), olivine (ol), mesostasis (ms), cr-spinels (Cr-Sp), on large scales. The images on the right highlight Fe–Ni grains in association with troilite (FeS) and cr-spinels.

(Einsle et al., 2016; Muxworthy & Williams, 2015). This observation also aligns with IRM unmixing results that indicated a population of HC components (>100 mT) for 10069 and 10071 (Figure 5; Table S6 in Supporting Information S1). Indeed, samples 10069 and 10071 belong to a different petrologic group (Group A) compared to the other samples 10003 and 10044 (Groups B1 and B2) (Beaty & Albee, 1980).

The intricate subgrain structure is especially prominent in sample 10071, which shows a previously unreported tangled lath microstructure in lunar metallic Fe (see additional examples in (Figure S23 in Supporting Information S1)). While the presence of impurities (e.g., Ni) might explain the observed lath texture, EDX elemental mapping did not reveal significant compositional differences (Figure 8). Instead, the differences in Fe brightness are attributed to variations in the crystallographic orientation of the subgrains. Alternatively, this lath structure could result from a rapid cooling rate, similar to the lath structures observed in synthetic martensitic steels (Shang et al., 2019). Notably, the Fe grains in sample 10071 are derived from a sheaf-like, finer-grained region of the overall basalt sample, likely reflecting rapid cooling effects (Drake & Weill, 1971).

5. Discussion

Origin of the magnetic transition at 120 K: As discussed in Section 4, no iron oxides were detected in our lunar basalt samples, apart from a 7–20 nm surface oxidation of our old thin sections. It is unlikely that such thin oxidized layers on the Fe–Ni alloys would be detectable using the MPMS system. In contrast, our bulk rock samples subjected to magnetic measurements were newer (prepared <5 years ago) and have a far smaller surface area to volume ratio than the thin sections.

As described in Section 2, the observed magnetic transition at 120 K is likely attributed to the chromite-ulvöspinel series. Previous studies on certain Apollo mare basalts (e.g., 10020, 12008, 12009, 12022, and 15597) have reported the presence of chromite-ulvöspinel series minerals (Haggerty et al., 1970; Neal et al., 1994; Weigand &

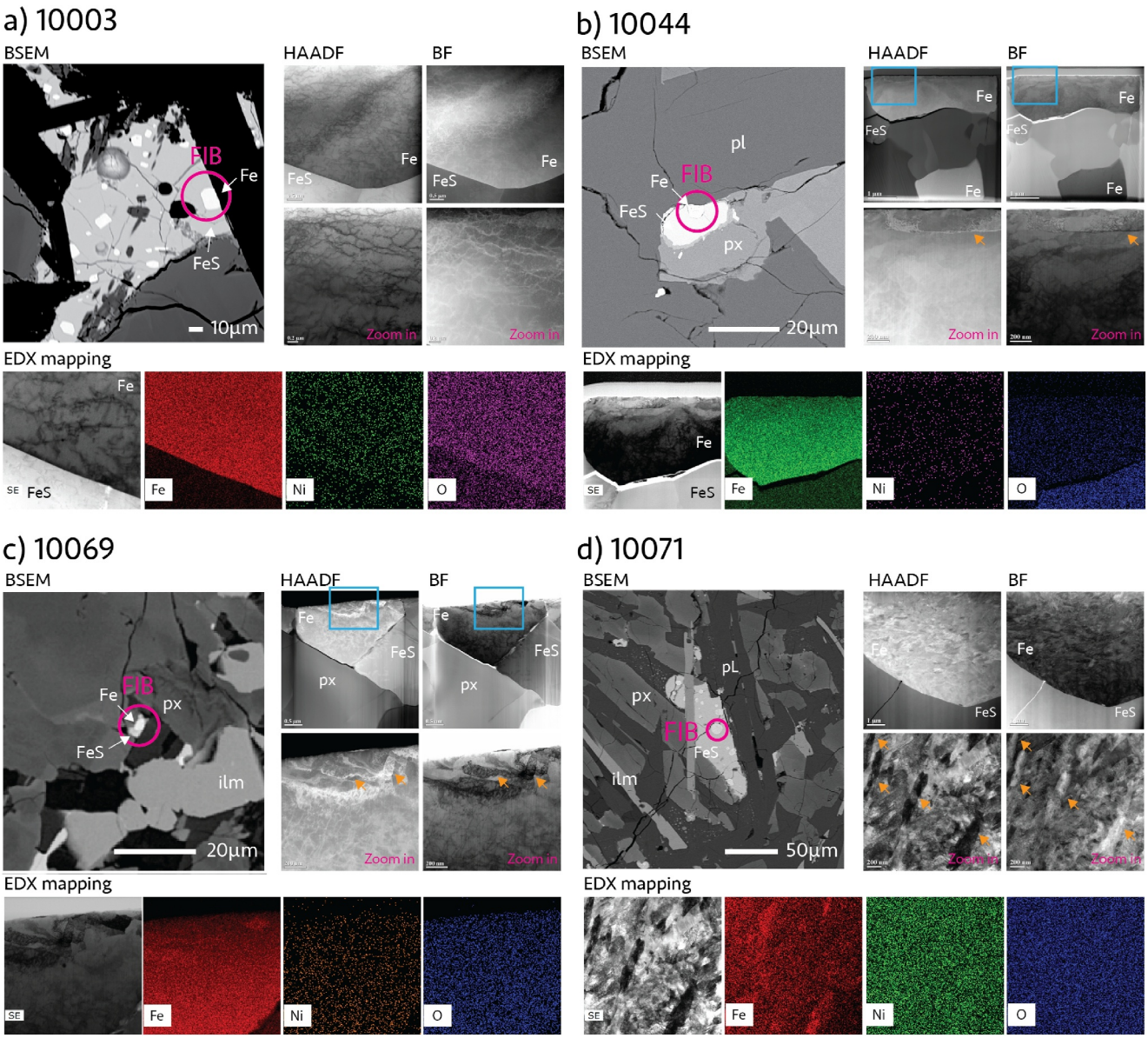

Figure 8. Backscattered scanning electron microscopy (BSEM) and transmission electron microscopy (TEM) imaging results showing kamacite grains in (a) 10003,184, (b) 10044,49, (c) 10069,33, (d) 10071,31. The left BSEM images show the area for focused ion beam (FIB) extraction for TEM analysis (indicated by pink circles), and the right images show high-angle annular dark-field (HAADF) and bright-field (BF) images of the extracted focused ion beam (FIB) section. The regions outlined by blue boxes on top panels are magnified in the figure below. Orange arrows indicate subgrain structures within the primary grains. The bottom panels for each sample provide EDX mapping at the target locations, showing elemental distribution for Fe, Ni, and O.

Hollister, 1973). Although these minerals were not initially identified in Apollo samples 10003, 10044, 10069, and 10071, our compositional analysis revealed trace amounts of ulvöspinel-chromite series in samples 10003 and 10044 (Figure S24 in Supporting Information S1). It is noted that high *K* Apollo 11 samples generally lack chromite and ulvöspinels (Warner et al., 1978), and co-crystallization of ilmenite and ulvöspinel is unlikely due to their significantly different stability curves as a function of temperature and oxygen pressure (Papike et al., 1991). This observation raises questions about potential changes in the oxygen fugacity conditions during the cooling of these basalts.

Our LT data for standard minerals (metallic Fe, ulvöspinel, iron chromite, and ilmenite), collected following the MPMS standard protocol from the Institute for Rock Magnetism, could serve as a valuable reference for interpreting LT magnetic measurements of extraterrestrial materials. While these data enable reliable qualitative

mineralogical analysis, several important limitations must be acknowledged when attempting quantitative interpretation. Under ideal conditions, mass-normalized samples enable quantitative estimation of modal abundances for phases exhibiting distinct low-temperature magnetic behavior. To test this approach, we conducted controlled mixing experiments using SD and MD iron and ulvöspinel combined with silicate powders, and found that spectral unmixing of these mixture curves yielded reasonable estimates of phase proportions (Text S5; Figures S25 and S26 in Supporting Information S1). However, applying this approach directly to natural rock samples remains challenging for several reasons: (a) LT magnetic behavior can vary significantly with grain size, as demonstrated by our results for Fe with different grain sizes (Section 2.3.1). (b) For some cases, magnetic interactions between grains may lead to complex, non-linear behavior that complicates interpretation (Text S5; Figure S25 in Supporting Information S1). (c) The magnetic transition temperatures of minerals can vary widely depending on elemental substitution (e.g., Ni content in metallic Fe (Kohout et al., 2007), or Cr content in chromite (Gattacceca et al., 2011; Hodel et al., 2020)). (d) Paramagnetic (sometimes ferromagnetic) silicate phases such as pyroxene and olivine can significantly affect the shape of J–T curves. Despite these limitations, rough estimation based on fitting to the FC curve for our Apollo 11 ilmenite basalts suggests that, assuming ilmenite constitutes 15%–20% of bulk mare basalt, the expected ulvöspinel content in such samples would be approximately 0.15%–0.4% by volume.

Fe–Ni alloys as paleomagnetic remanence carriers: Prior research suggests that unshocked mare basalts are an optimal choice for studying lunar paleomagnetism. They likely cooled slowly enough to preclude the recording of thermal remanent magnetization from impact-generated magnetic fields which are generally expected to persist for $\ll$1 day (Chaffee et al., 2023; Crawford, 2020; Hood & Artemieva, 2008). As long as there is no microscopic evidence of shock (limiting peak pressures to <5 GPa), the higher coercivity components used for paleointensity calculations are expected to be largely unaffected by shock remagnetization or demagnetization via impact events (Bezaeva et al., 2022; Stöffler et al., 2006, 2018; Tikoo et al., 2015). Viscous remanent magnetization due to the Earth's magnetic field over a few decades is also not a significant concern for these samples (Dunlop, 1973; Weiss & Tikoo, 2014). A recent study shows that potential magnetic contamination in lunar mare basalts, such as exposure to magnetic fields during spacecraft transit or certain laboratory procedures, can also be effectively cleaned (Tikoo & Jung, 2023). In this study, we further demonstrate that this HC range is also resistant to low temperatures and is not affected by lunar diurnal temperature cycles. Apart from microscopy evidence suggesting Fe–Ni subgrains within the iron-troilite eutectic assemblages that we report in this study and in Jung et al. (2024), conclusive identification of SD grains within mare basalts remains limited. Even detailed recent SEM analyses have shown that the smallest discernible isolated Fe–Ni grains are larger than 100 nm in diameter for spherical grains and larger than 200 nm for elongated grains (Figures referenced from the Supporting Information of Zhou et al. (2024)), placing them within the MD grain size range for iron (Einsle et al., 2016; Muxworthy & Williams, 2015).

We note the paleointensity fidelity limit value (i.e., the minimum paleofield from which a reliable paleointensity may be retrieved from a sample using the ARM and IRM paleointensity methods; see Tikoo et al. (2012, 2014) for definitions) reported for samples with small subgrains (7.69 μT for samples 10069 and 10071) was lower than that for samples without any subgrains (23.07 μT for samples 10003 and 10044) (Jung et al., 2024). Our observations raise the possibility that samples exhibiting the Fe–Ni subgrain microstructure in TEM imaging may be better paleofield recorders than samples without them. These subgrains have the potential to effectively record ancient lunar dynamo fields and resist secondary remagnetization events. Key questions for future research include determining the effect of magnetic interactions between subgrains on their magnetic properties, their ability to retain thermal remanent magnetization, and the processes that lead to their microstructure formation.

6. Conclusion

We investigated the cryogenic magnetic properties and conducted detailed microscopy on Apollo lunar mare basalts to improve our understanding of their magnetic mineralogy and its implications for paleointensity retrieval. Our observations raise four key points: (a) We identified distinct magnetic transitions in lunar mare basalts at characteristic temperatures: below 30 K (ilmenite), 60–80 K (chromite and possibly troilite), and around 120 K, the latter of which is more consistent with ulvöspinel/chromite than magnetite. (b) Electron microscopy analysis revealed no evidence of secondary iron oxides such as magnetite in our samples. While minor surface-level oxidation was observed, this does not affect the bulk magnetic properties, confirming that the predominant magnetic carriers are metallic Fe–Ni alloys as reported in many other lunar magnetism studies. (c) Our TEM

observations revealed likely SD subgrains within larger Fe grains, potentially explaining the HC magnetic components observed in these samples. (d) This HC component resists demagnetization during extreme lunar diurnal temperature variations, suggesting it is unlikely to be significantly altered by temperature cycling. This indicates that the HC component may retain the capacity to record ancient dynamo fields and serves as a reliable target for paleointensity estimates in mare basalts.

Data Availability Statement

BSEM, EDS, FORC, magnetic hysteresis, IRM unmixing, low-temperature paleomagnetic measurements, TEM, MPMS, and WDS data from this study are available on Zenodo, a permanent CERN-backed online data repository (Jung & Tikoo, 2025).

The low-temperature paleomagnetic measurements are available in the Magnetics Information Consortium (MagIC) database (earthref.org/MagIC/20328 or https://doi.org/10.7288/V4/MAGIC/20328).

Acknowledgments

We thank J. Gattacceca and the anonymous reviewer for their constructive feedback and insightful suggestions. We extend our gratitude to R. Ziegler and J. Gross, CAPTEM, and the Lunar Receiving Laboratory at the Johnson Space Center for their efforts in allocating and preparing our samples. We are also thankful to H. Yang from Stanford University for laboratory assistance with rock magnetic measurements. At the Washington University in St. Louis, we appreciate H. Li from the Institute of Materials Science and Engineering for TEM assistance, H. Craigg from the Department of Earth, Environmental, and Planetary Sciences for synthesizing chromite samples, and Y. Shi and C. Zu from the Department of Physics for laboratory assistance. We acknowledge the Institute for Rock Magnetism at the University of Minnesota for awarding a Visiting Fellow grant to J. Jung. The Institute for Rock Magnetism is a US National Multi-user Facility supported through the Instrumentation and Facilities program of the National Science Foundation, Earth Sciences Division (EAR-2153786), and by funding from the University of Minnesota. Special thanks to B. Moskowitz at IRM for insightful discussions on low-temperature measurement results. Part of this work was performed at the Stanford Nano Shared Facilities (SNSF) RRID:SCR_023230, supported by the National Science Foundation under award ECCS-2026822. This research was supported by NASA award numbers 80NSSC20K1528, 80NSSC21K1541, 80NSSC20K0640, and 80NSSC23M0161, as well as a Stanford Doerr School of Sustainability Discovery Grant.

References

Antretter, M., Fuller, M., Scott, E., Jackson, M., Moskowitz, B., & Solheid, P. (2003). Paleomagnetic record of Martian meteorite Alh84001. *Journal of Geophysical Research*, *108*(E6). https://doi.org/10.1029/2002JE001979

Banerjee, S. K. (1972). Iron-titanium-chromite, a possible new carrier of remanent magnetization in lunar rocks. *Lunar and Planetary Science Conference Proceedings*, *3*, 2337.

Beaty, D. W., & Albee, A. L. (1980). The geology and petrology of the Apollo 11 landing site. *Lunar and Planetary Science Conference Proceedings*, *1*, 23–35.

Besnus, M., & Meyer, A. (1964). Nouvelles données expérimentales sur le magnétisme de la pyrrhotine naturelle. In *Proceedings International Conference magazine* (Vol. 20).

Bezaeva, N., Gattacceca, J., Rochette, P., & Sadykov, R. (2022). Demagnetization of ordinary chondrites under hydrostatic pressure up to 1.8 gpa. *Geochemistry International*, *60*(5), 421–429. https://doi.org/10.1134/S0016702922050032

Bilardello, D., & Jackson, M. (2013). IRM quarterly, volume 23, number 3 (fall 2013). *Cover Article: What do the Mumpsies do? IRM Quarterly*, *23*(3).

Burton, B., Robinson, P., McEnroe, S., Fabian, K., & Ballar, T. (2008). A low-temperature phase diagram for ilmenite-rich compositions in the system Fe_2O_3–$FeTiO_3$. *American Mineralogist*, *93*(8–9), 1260–1272. https://doi.org/10.2138/am.2008.2690

Cai, S., Qi, K., Yang, S., Fang, J., Shi, P., Shen, Z., et al. (2024). A reinforced lunar dynamo recorded by Chang'e-6 Farside basalt. *Nature*, *643*(8071), 361–365. https://doi.org/10.1038/s41586-024-08526-2

Cameron, E. N. (1970). Opaque minerals in lunar samples. *Science*, *167*(3918), 623–625. https://doi.org/10.1126/science.167.3918.623

Cao, Z., Guo, Z., Li, C., Zhao, S., Li, Y., He, Q., et al. (2024). Submicroscopic magnetite May be ubiquitous in the lunar regolith of the high-Ti region. *Science Advances*, *10*(38), eadn2301. https://doi.org/10.1126/sciadv.adn2301

Chaffee, T. M., Tikoo, S., Boeschen, S. G., Abubo, R., Jung, J.-I., & Weiss, B. P. (2023). No evidence of magnetization from impact-generated fields in 2 ma lunar impact melt glasses. *AGU23*.

Chowdhary, S., Collinson, D., Stephenson, A., & Runcorn, S. (1987). Further investigations into lunar palaeointensity determinations. *Physics of the Earth and Planetary Interiors*, *49*(1), 133–141. https://doi.org/10.1016/0031-9201(87)90137-3

Cornell, R., & Schwertmann, U. (2003). Introduction to the iron oxides. In *The iron oxides* (pp. 1–7). John Wiley & Sons, Ltd. https://doi.org/10.1002/3527602097.ch1

Cottrell, R. D., Zhou, T., & Tarduno, J. A. (2024). Dataset of replicate Apollo sample magnetizations bearing on impacts and absence of a long-lived lunar dynamo. *Scientific Data*, *11*(1), 807. https://doi.org/10.1038/s41597-024-03626-0

Cournède, C., Gattacceca, J., & Rochette, P. (2012). Magnetic study of large Apollo samples: Possible evidence for an ancient centered dipolar field on the moon. *Earth and Planetary Science Letters*, *331–332*, 31–42. https://doi.org/10.1016/j.epsl.2012.03.004

Crawford, D. A. (2020). Simulations of magnetic fields produced by asteroid impact: Possible implications for planetary Paleomagnetism. *International Journal of Impact Engineering*, *137*, 103464. https://doi.org/10.1016/j.ijimpeng.2019.103464

Cuda, J., Kohout, T., Tucek, J., Haloda, J., Filip, J., Prucek, R., & Zboril, R. (2011). Low-temperature magnetic transition in Troilite: A simple marker for highly stoichiometric FES systems. *Journal of Geophysical Research*, *116*(B11). https://doi.org/10.1029/2011JB008232

Drake, M., & Weill, D. (1971). Petrology of Apollo 11 sample 10071. A differentiated mini-igneous complex. *Earth and Planetary Science Letters*, *13*(1), 61–70. https://doi.org/10.1016/0012-821X(71)90105-1

Dunlop, D. J. (1973). Theory of the magnetic viscosity of lunar and terrestrial rocks. *Reviews of Geophysics*, *11*(4), 855–901. https://doi.org/10.1029/RG011i004p00855

Dunlop, D. J. (2003). Stepwise and continuous low-temperature demagnetization. *Geophysical Research Letters*, *30*(11). https://doi.org/10.1029/2003GL017268

Einsle, J. F., Harrison, R. J., Kasama, T., Conbhuí, P. Ó., Fabian, K., Williams, W., et al. (2016). Multi-scale three-dimensional characterization of iron particles in dusty olivine: Implications for paleomagnetism of chondritic meteorites. *American Mineralogist*, *101*(9), 2070–2084. https://doi.org/10.2138/am-2016-5738ccby

Engelmann, R., Kontny, A., & Lattard, D. (2010). Low-temperature magnetism of synthetic Fe–Ti oxide assemblages. *Journal of Geophysical Research*, *115*(B12). https://doi.org/10.1029/2010JB000865

Fillion, G., & Rochette, P. (1988). The low temperature transition in monoclinic Pyrrhotite. *Journal de Physique. Colloques*, *49*(C8), C8-907–908. https://doi.org/10.1051/jphyscol:19888412

Forester, D. W., Marquardt, C. L., & Griscom, D. L. (1973). Mossbauer search for ferric oxide phases in lunar materials and simulated lunar materials. In *Lunar and Planetary Science Conference* (Vol. 4).257.

Fuller, M. (1974). Lunar magnetism. *Reviews of Geophysics*, *12*(1), 23–70. https://doi.org/10.1029/RG012i001p00023

Gattacceca, J., Rochette, P., Lagroix, F., Mathé, P.-E., & Zanda, B. (2011). Low temperature magnetic transition of chromite in ordinary chondrites. *Geophysical Research Letters*, *38*(10). https://doi.org/10.1029/2011GL047173

Gibb, F., Stumpfl, E., & Zussman, J. (1970). Opaque minerals in an Apollo 12 rock. *Earth and Planetary Science Letters*, *9*(3), 217–224. https://doi.org/10.1016/0012-821X(70)90031-2

Guo, Z., Li, C., Li, Y., Wen, Y., Wu, Y., Jia, B., et al. (2022). Sub-microscopic magnetite and metallic iron particles formed by eutectic reaction in Chang'e-5 lunar soil. *Nature Communications*, *13*(1), 7177. https://doi.org/10.1038/s41467-022-35009-7

Haggerty, S. E. (1971). Compositional variations in lunar Spinels. *Nature; Physical Science*, *233*(43), 156–160. https://doi.org/10.1038/physci233156a0

Haggerty, S. E. (1978). The redox state of planetary basalts. *Geophysical Research Letters*, *5*(6), 443–446. https://doi.org/10.1029/GL005i006p00443

Haggerty, S. E., Boyd, F. R., Bell, P. M., Finger, L. W., & Bryan, W. B. (1970). Opaque minerals and olivine in lavas and Breccias from mare tranquillitatis. In *Geochimica et Cosmochimica Acta Supplement, Volume 1. Proceedings of the Apollo 11 Lunar Science Conference* (Vol. 1). (Mineraolgy and Petrology). (p. 513).

Halgedahl, S. L., & Jarrard, R. D. (1995). Low-temperature behavior of single-domain through multidomain magnetite. *Earth and Planetary Science Letters*, *130*(1), 127–139. https://doi.org/10.1016/0012-821X(94)00260-6

Harrison, R. J. (2009). Magnetic ordering in the ilmenite-hematite solid solution: A computational study of the low-temperature spin glass region. *Geochemistry, Geophysics, Geosystems*, *10*(2). https://doi.org/10.1029/2008GC002240

Harrison, R. J., & Feinberg, J. M. (2008). Forcinel: An improved algorithm for calculating first-order reversal curve distributions using locally weighted regression smoothing. *Geochemistry, Geophysics, Geosystems*, *9*(5). https://doi.org/10.1029/2008GC001987

Hodel, F., Macouin, M., Trindade, R. I. F., Araujo, J. F. D. F., Respaud, M., Meunier, J. F., et al. (2020). Magnetic properties of ferritchromite and Cr-magnetite and monitoring of Cr-spinels alteration in ultramafic and mafic rocks. *Geochemistry, Geophysics, Geosystems*, *21*(11), e2020GC009227. https://doi.org/10.1029/2020GC009227

Hodych, J. P., Mackay, R. I., & English, G. M. (1998). Low-temperature demagnetization of saturation remanence in magnetite-bearing dolerites of high coercivity. *Geophysical Journal International*, *132*(2), 401–411. https://doi.org/10.1046/j.1365-246x.1998.00445.x

Hood, L. L., & Artemieva, N. A. (2008). Antipodal effects of lunar basin-forming impacts: Initial 3d simulations and comparisons with observations. *Icarus*, *193*(2), 485–502. (Saturn's Icy Satellites from Cassini). https://doi.org/10.1016/j.icarus.2007.08.023

Horstmann, M., Humayun, M., Harries, D., Langenhorst, F., Chabot, N. L., Bischoff, A., & Zolensky, M. E. (2013). Wüstite in the fusion crust of Almahata Sitta sulfide-metal assemblage MS-166: Evidence for oxygen in metallic melts. *Meteoritics & Planetary Sciences*, *48*(5), 730–743. https://doi.org/10.1111/maps.12097

Ishikawa, Y. (1967). Magnetic properties of a single crystal of Fe_2TiO_4. *Physics Letters A*, *24*(13), 725–727. https://doi.org/10.1016/0375-9601(67)90236-8

Ishikawa, Y., Sato, S., & Syono, Y. (1971). Neutron and magnetic studies of a single crystal of Fe_2TiO_4. *Journal of the Physical Society of Japan*, *31*(2), 452–460. https://doi.org/10.1143/JPSJ.31.452

Jackson, M., & Solheid, P. (2010). On the quantitative analysis and evaluation of magnetic hysteresis data. *Geochemistry, Geophysics, Geosystems*, *11*(4). https://doi.org/10.1029/2009GC002932

Jedwab, J., Herbosch, A., Wollast, R., Naessens, G., & Geen-Peers, N. V. (1970). Search for magnetite in lunar rocks and fines. *Science*, *167*(3918), 618–619. https://doi.org/10.1126/science.167.3918.618

Joy, K. H., Visscher, C., Zolensky, M. E., Mikouchi, T., Hagiya, K., Ohsumi, K., & Kring, D. A. (2015). Identification of magnetite in lunar regolith breccia 60016: Evidence for oxidized conditions at the lunar surface. *Meteoritics & Planetary Sciences*, *50*(7), 1157–1172. https://doi.org/10.1111/maps.12462

Jung, J. I., & Tikoo, S. (2025). Magnetic Mineralogy in Lunar Mare Basalts and Implications for Paleointensity Retrieval [Dataset]. *Zenodo*. https://doi.org/10.5281/zenodo.14920646

Jung, J.-I., Tikoo, S. M., Burns, D., Váci, Z., & Krawczynski, M. J. (2024). Assessing lunar paleointensity variability during the 3.9–3.5 ga high field epoch. *Earth and Planetary Science Letters*, *638*, 118757. https://doi.org/10.1016/j.epsl.2024.118757

Kohout, T., Kosterov, A., Jackson, M., Pesonen, L., Kletetschka, G., & Lehtinen, M. (2007). Low-temperature magnetic properties of the neuschwanstein El6 meteorite. *Earth and Planetary Science Letters*, *261*(1), 143–151. https://doi.org/10.1016/j.epsl.2007.06.022

Li, S., Lucey, P. G., Fraeman, A. A., Poppe, A. R., Sun, V. Z., Hurley, D. M., & Schultz, P. H. (2020). Widespread hematite at high latitudes of the moon. *Science Advances*, *6*(36), eaba1940. https://doi.org/10.1126/sciadv.aba1940

Liang, Y., Tikoo, S. M., & Krawczynski, M. J. (2024). Possibility of lunar crustal magmatism producing strong crustal magnetism. *Journal of Geophysical Research: Planets*, *129*(5), e2023JE008179. https://doi.org/10.1029/2023JE008179

Liu, J., Long, Y., Bai, D., Sun, H., Zhang, H., Long, K., & Yan, T. (2019). Magnetic properties of Feni alloys for high-temperature thermomagnetic power generation. *AIP Advances*, *9*(4), 045227. https://doi.org/10.1063/1.5086411

Maxbauer, D. P., Feinberg, J. M., & Fox, D. L. (2016). Max UNMIX: A web application for unmixing magnetic coercivity distributions. *Computers & Geosciences*, *95*, 140–145. https://doi.org/10.1016/j.cageo.2016.07.009

McCammon, C. (1992). Magnetic properties of Fexo (x 0.95): Variation of NEEL temperature. *Journal of Magnetism and Magnetic Materials*, *104–107*, 1937–1938. https://doi.org/10.1016/0304-8853(92)91612-W

Morin, F. J. (1950). Magnetic susceptibility of αFe_2O_3 and αFe_2O_3 with added titanium. *Physics Reviews*, *78*(6), 819–820. https://doi.org/10.1103/PhysRev.78.819.2

Muxworthy, A. R., & Williams, W. (2015). Critical single-domain grain sizes in elongated iron particles: Implications for meteoritic and lunar magnetism. *Geophysical Journal International*, *202*(1), 578–583. https://doi.org/10.1093/gji/ggv180

Nagata, T., Ishikawa, Y., Kinoshita, H., Kono, M., Syono, Y., & Fisher, R. M. (1970). Magnetic properties of the lunar crystalline rock and fines. *Science*, *167*(3918), 703–704. https://doi.org/10.1126/science.167.3918.703

Nagata, T., Kobayashi, K., & Fuller, M. D. (1964). Identification of magnetite and hematite in rocks by magnetic observation at low temperature. *Journal of Geophysical Research (1896–1977)*, *69*(10), 2111–2120. https://doi.org/10.1029/JZ069i010p02111

Nakamura, S., & Fuwa, A. (2014). Local and dynamic Jahn-teller distortion in Ulvöspinel Fe_2TiO_4. *Hyperfine Interactions*, *226*(1–3), 267–274. https://doi.org/10.1007/s10751-013-0921-7

Neal, C. R., Hacker, M. D., Snyder, G. A., Taylor, L. A., Liu, Y.-G., & Schmitt, R. A. (1994). Basalt generation at the Apollo 12 site. Part 1: New data, classification, and re-evaluation. *Meteoritics*, *29*(3), 334–348. https://doi.org/10.1111/j.1945-5100.1994.tb00597.x

Nichols, C. I. O., Weiss, B. P., Getzin, B. L., Schmitt, H. H., Béguin, A., Rae, A. S. P., & Shah, J. (2021). The palaeoinclination of the ancient lunar magnetic field from an Apollo 17 basalt. *Nature Astronomy*, *5*(12), 1216–1223. https://doi.org/10.1038/s41550-021-01469-y

Papike, J., Taylor, L., & Simon, S. (1991). Lunar minerals. In G. H. Heiken, D. T. Vaniman, & B. M. French (Eds.), *Lunar sourcebook, a user's guide to the moon* (pp. 121–181).

Pearce, G. W., Hoye, G. S., Strangway, D. W., Walker, B. M., & Taylor, L. A. (1976). Some complexities in the determination of lunar paleointensities. In *Proceedings of the Lunar Science Conference, 7th, Houston, tex., March 15-19, 1976* (Vol. 3, pp. 3271–3297). Research supported by the National Research Council of Canada.

Readman, R. (1978). Magnetic properties of Ulvöspinel. *Physics of the Earth and Planetary Interiors*, *16*(3), 196–199. https://doi.org/10.1016/0031-9201(78)90011-0

Reid, A. M., Meyer, C., Harmon, R. S., & Brett, R. (1970). Metal grains in Apollo 12 igneous rocks. *Earth and Planetary Science Letters*, *9*(1), 1–5. https://doi.org/10.1016/0012-821X(70)90015-4

Robbins, M., Wertheim, G., Sherwood, R., & Buchanan, D. (1971). Magnetic properties and site distributions in the system $FeCr_2O_4$–Fe_3O_4 (Fe_2+Cr_2–XFe_3+O_4). *Journal of Physics and Chemistry of Solids*, *32*(3), 717–729. https://doi.org/10.1016/S0022-3697(71)80412-2

Runcorn, S. K., Collinson, D. W., Reilly, W. O., Stephenson, A., Battey, M. H., Manson, A. J., & Readman, P. W. (1971). Magnetic properties of Apollo 12 lunar samples. *Proceedings of the Royal Society of London. A. Mathematical and Physical Sciences*, *325*(1561), 157–174. https://doi.org/10.1098/rspa.1971.0163

Senftle, F. E., Thorpe, A. N., Briggs, C., Alexander, C., Minkin, J., & Griscom, D. L. (1975). The NÉEL transition and magnetic properties of terrestrial, synthetic, and lunar ilmenites. *Earth and Planetary Science Letters*, *26*(3), 377–386. https://doi.org/10.1016/0012-821X(75)90014-X

Shang, Z., Ding, J., Fan, C., Song, M., Li, J., Li, Q., et al. (2019). Tailoring the strength and ductility of T91 steel by partial tempering treatment. *Acta Materialia*, *169*, 209–224. https://doi.org/10.1016/j.actamat.2019.02.043

Shea, E. K., Weiss, B. P., Cassata, W. S., Shuster, D. L., Tikoo, S. M., Gattacceca, J., et al. (2012). A long-lived lunar core dynamo. *Science*, *335*(6067), 453–456. https://doi.org/10.1126/science.1215359

Skinner, B. J. (1970). High crystallization temperatures indicated for igneous rocks from tranquillity base. *Science*, *167*(3918), 652–654. https://doi.org/10.1126/science.167.3918.652

Smirnov, A. V. (2009). Grain size dependence of low-temperature remanent magnetization in natural and synthetic magnetite: Experimental study. *Earth Planets and Space*, *61*(1), 119–124. https://doi.org/10.1186/BF03352891

Stöffler, D., Hamann, C., & Metzler, K. (2018). Shock metamorphism of planetary silicate rocks and sediments: Proposal for an updated classification system. *Meteoritics & Planetary Sciences*, *53*(1), 5–49. https://doi.org/10.1111/maps.12912

Stöffler, D., Ryder, G., Ivanov, B. A., Artemieva, N. A., Cintala, M. J., & Grieve, R. A. F. (2006). Cratering history and lunar chronology. *Reviews in Mineralogy and Geochemistry*, *60*(1), 519–596. https://doi.org/10.2138/rmg.2006.60.05

Strauss, B. E., Tikoo, S. M., Gross, J., Setera, J. B., & Turrin, B. (2021). Constraining the decline of the lunar dynamo field at ≈3.1 ga through paleomagnetic analyses of Apollo 12 mare basalts. *Journal of Geophysical Research: Planets*, *126*(3), e2020JE006715. https://doi.org/10.1029/2020JE006715

Suavet, C., Weiss, B. P., Cassata, W. S., Shuster, D. L., Gattacceca, J., Chan, L., et al. (2013). Persistence and origin of the lunar core dynamo. *Proceedings of the National Academy of Sciences*, *110*(21), 8453–8458. https://doi.org/10.1073/pnas.1300341110

Tarduno, J. A., Cottrell, R. D., Lawrence, K., Bono, R. K., Huang, W., Johnson, C. L., et al. (2021). Absence of a long-lived lunar paleomagnetosphere. *Science Advances*, *7*(32), eabi7647. https://doi.org/10.1126/sciadv.abi7647

Tauxe, L. (2008). *Essentials of rock and paleomagnetism*. Scripps Institution of Oceanography. (With contributions from Subir K. Banerjee, Robert F. Butler, and Rob van der Voo).

Tikoo, S. M., & Evans, A. J. (2022). Dynamos in the inner solar system. *Annual Review of Earth and Planetary Sciences*, *50*(1), 99–122. https://doi.org/10.1146/annurev-earth-032320-102418

Tikoo, S. M., Gattacceca, J., Swanson-Hysell, N. L., Weiss, B. P., Suavet, C., & Cournède, C. (2015). Preservation and detectability of shock-induced magnetization. *Journal of Geophysical Research: Planets*, *120*(9), 1461–1475. https://doi.org/10.1002/2015JE004840

Tikoo, S. M., & Jung, J. (2023). Establishing a lunar origin for paleomagnetic records in Apollo samples. *Geophysical Research Letters*, *50*(19), e2023GL105152. https://doi.org/10.1029/2023GL105152

Tikoo, S. M., Weiss, B. P., Buz, J., Lima, E. A., Shea, E. K., Melo, G., & Grove, T. L. (2012). Magnetic fidelity of lunar samples and implications for an ancient core dynamo. *Earth and Planetary Science Letters*, *337–338*, 93–103. https://doi.org/10.1016/j.epsl.2012.05.024

Tikoo, S. M., Weiss, B. P., Cassata, W. S., Shuster, D. L., Gattacceca, J., Lima, E. A., et al. (2014). Decline of the lunar core dynamo. *Earth and Planetary Science Letters*, *404*, 89–97. https://doi.org/10.1016/j.epsl.2014.07.010

Tikoo, S. M., Weiss, B. P., Shuster, D. L., Suavet, C., Wang, H., & Grove, T. L. (2017). A two-billion-year history for the lunar dynamo. *Science Advances*, *3*(8), e1700207. https://doi.org/10.1126/sciadv.1700207

Verwey, E., & Haayman, P. (1941). Electronic conductivity and transition point of magnetite ("Fe_3O_4"). *Physica*, *8*(9), 979–987. https://doi.org/10.1016/S0031-8914(41)80005-6

Wadhwa, M. (2008). Redox conditions on small bodies, the moon and Mars. *Reviews in Mineralogy and Geochemistry*, *68*(1), 493–510. https://doi.org/10.2138/rmg.2008.68.17

Walz, F. (2002). The verwey transition—A topical review. *Journal of Physics: Condensed Matter*, *14*(12), R285–R340. https://doi.org/10.1088/0953-8984/14/12/203

Warner, R. D., Nehru, C. E., & Keil, K. (1978). Opaque oxide mineral crystallization in lunar high-titanium mare basalts. *American Mineralogist*, *63*(11–12), 1209–1224.

Wei, Q., Gilder, S. A., & Maier, B. (2014). Pressure dependence on the remanent magnetization of Fe–Ni alloys and Ni metal. *Physical Review B: Condensed Matter*, *90*(14), 144425. https://doi.org/10.1103/PhysRevB.90.144425

Weigand, P., & Hollister, L. (1973). Basaltic vitrophyre 15597: An undifferentiated melt sample. *Earth and Planetary Science Letters*, *19*(1), 61–74. https://doi.org/10.1016/0012-821X(73)90178-7

Weiss, B. P., Kim, S. S., Kirschvink, J. L., Kopp, R. E., Sankaran, M., Kobayashi, A., & Komeili, A. (2004). Magnetic tests for magnetosome chains in Martian meteorite alh84001. *Proceedings of the National Academy of Sciences*, *101*(22), 8281–8284. https://doi.org/10.1073/pnas.0402292101

Weiss, B. P., & Tikoo, S. M. (2014). The lunar dynamo. *Science*, *346*(6214), 1246753. https://doi.org/10.1126/science.1246753

Wieczorek, M. A., Weiss, B. P., Breuer, D., Cébron, D., Fuller, M., Garrick-Bethell, I., et al. (2023). Lunar magnetism. *Reviews in Mineralogy and Geochemistry*, *89*(1), 207–241. https://doi.org/10.2138/rmg.2023.89.05

Williams, J.-P., Paige, D., Greenhagen, B., & Sefton-Nash, E. (2017). The global surface temperatures of the moon as measured by the diviner lunar radiometer experiment. *Icarus*, *283*, 300–325. (Lunar Reconnaissance Orbiter—Part II). https://doi.org/10.1016/j.icarus.2016.08.012

Yamamoto, Y., Tsunakawa, H., & Shibuya, H. (2003). Palaeointensity study of the Hawaiian 1960 lava: Implications for possible causes of erroneously high intensities. *Geophysical Journal International*, *153*(1), 263–276. https://doi.org/10.1046/j.1365-246X.2003.01909.x

Zhou, T., Tarduno, J. A., Cottrell, R. D., Neal, C. R., Nimmo, F., Blackman, E. G., & Ibañez-Mejia, M. (2024). A lunar core dynamo limited to the moon's first approximately 140 million years. *Communications Earth & Environment*, *5*(1), 456. https://doi.org/10.1038/s43247-024-01551-z